

# Joint modeling of the probability distribution and power spectrum of the Ly $\alpha$ forest : comparison with observations at $z = 3$

Vincent Desjacques<sup>1</sup> and Adi Nusser<sup>1,2</sup>

<sup>1</sup> The Physics Department and the Asher Space Research Institute, Technion, Haifa 32000, Israel

<sup>2</sup> The Institute for Advanced Study, School of Natural Sciences, Einstein Drive, Princeton, NJ 08540

Email : dvince@physics.technion.ac.il, adi@physics.technion.ac.il

29 August 2018

## ABSTRACT

We present results of joint modeling of the probability distribution function (PDF) and the one-dimensional power spectrum (PS) of the Ly $\alpha$  forest flux decrement. The sensitivity of these statistical measures to the shape and amplitude of the linear matter power spectrum is investigated using N-body simulations of two variants of the  $\Lambda$ CDM cosmology. In the first model, the linear power spectrum has a scale-invariant spectral index  $n_s = 1$ , whereas in the second, it has a negative running index (RSI),  $dn/dlnk < 0$ . We generate mock catalogs of QSO spectra, and compare their statistical properties to those of the observations at  $z = 3$ . We perform a joint fit of the power spectrum and the PDF. A scale-invariant model with  $\sigma_8 = 0.9$  matches well the data if the mean IGM temperature is  $T \lesssim 1.5 \times 10^4$  K. For higher temperature, it tends to overestimate the flux power spectrum over scales  $k \lesssim 0.01$  s km $^{-1}$ . The discrepancy is less severe when the PS alone is fitted. However, models matching the PS alone do not yield a good fit to the PDF. A joint analysis of the flux PS and PDF tightens the constraints on the model parameters and reduces systematic biases. The RSI model is consistent with the observed PDF and PS only if the temperature is  $T \gtrsim 2 \times 10^4$  K. The best fit models reproduce the slope and normalisation of the column density distribution, irrespective of the shape and amplitude of the linear power spectrum. They are also consistent with the observed line-width distribution given the large uncertainties. Our joint analysis suggests that  $\sigma_8$  is likely to be in the range 0.7–0.9 for a temperature  $1 \lesssim T \lesssim 2 \times 10^4$  K and a reasonable reionization history.

**Key words:** cosmology: theory – gravitation – dark matter – baryons – intergalactic medium

## 1 INTRODUCTION

Absorption features in the Ly $\alpha$  forest provide direct information on the large scale distribution of neutral hydrogen in the highly ionized intergalactic medium (Bahcall & Salpeter 1965; Gunn & Peterson 1965; see e.g. Rauch 1998 for a review). The Ly $\alpha$  forest is believed to originate in a warm photoionized, fluctuating intergalactic medium (IGM) which smoothly traces the distribution of the dark matter. This picture is sustained by hydrodynamical simulations and semi-analytical models which have succeeded in reproducing the observed statistics of the absorption lines and transmitted flux (e.g. McGill 1990; Bi 1993; Cen *et al.* 1994; Zhang, Anninos & Norman 1995; Petitjean, Mucket & Kates 1995; Hernquist *et al.* 1996; Katz *et al.* 1996; Miralda-

Escudé *et al.* 1996; Hui, Gnedin & Zhang 1997; Theuns *et al.* 1998; Schaye 2001). The Ly $\alpha$  forest can therefore serve as a probe the physical state of the IGM, and the underlying matter distribution over a wide range of scales and redshifts (e.g. Croft *et al.* 1998; Nusser & Haehnelt 2000; Schaye *et al.* 2000). Several method have been proposed for recovering the shape and amplitude of the primordial power spectrum,  $\Delta_L^2(k)$  (e.g. Croft *et al.* 1998, 2002b; McDonald *et al.* 2000; McDonald 2003). The current methods rely either on an inversion of the one-dimensional flux power spectrum  $\Delta_F^2(k)$  (e.g. Croft *et al.* 1999, 2002b; McDonald 2003), or on a forward comparison between the data and the simulations (e.g. Zaldarriaga, Hui & Tegmark 2001; McDonald *et al.* 2004b). The nonlinear relation between the matter and flux power spectra is calibrated by means of detailed nu-

numerical simulations (e.g. Croft *et al.* 1998; McDonald 2003). These methods are fundamentally limited by continuum fitting errors, metal contamination and nonlinear corrections (e.g. Hui *et al.* 2001; Zaldarriaga, Scoccimarro & Hui 2003; see also Gnedin & Hamilton 2002). Furthermore, one has to marginalize over the ‘nuisance’ parameters in order to place constraints on the spectral index  $n_s$  and the power spectrum normalisation amplitude  $\sigma_8$ . Underestimating the mean flux level  $\langle F \rangle$ , for example, can strongly bias the results as it was shown by Seljak, McDonald & Makarov (2003), and Viel, Haehnelt & Springel (2004). The most recent analyses of the Ly $\alpha$  forest favour a simple scale-invariant model with  $\sigma_8$  in the range 0.85–0.95 (McDonald *et al.* 2004b; Viel, Haehnelt & Springel 2004; Viel, Weller & Haehnelt 2004; Seljak *et al.* 2004). However, one should emphasize that these studies do not include in their analysis other statistics than the power spectrum of the Ly $\alpha$  forest. A priori, a model which fits the observed power spectrum solely will not necessarily agree with the observed PDF, bispectrum etc. It is therefore prudent to examine how other statistical measures of the forest constrain the cosmological model.

In this work, we follow a different strategy and assess the validity of a cosmological model using three statistical measures of the Ly $\alpha$  forest. These statistics are the one-dimensional flux power spectrum,  $\Delta_F^2(k)$ , the flux probability distribution function (PDF),  $P(F)$ , and the neutral hydrogen column density distribution  $f(N_{\mathrm{HI}})$ . Furthermore, we adopt the “forward approach” which consists in comparing the observed statistical measures with those directly derived from N-body simulations of the cosmological model under consideration (see e.g. Zaldarriaga, Hui & Tegmark 2001). This approach has the advantage that it does not require any inversion procedure to obtain the linear mass power spectrum.

Combining several statistical measures could significantly affect the constraints on the shape and amplitude of the primordial power spectrum as inferred from  $\Delta_F^2(k)$  alone. In this study, we will attempt to match simultaneously the three statistics mentioned above. In principle, higher order correlations such as the bispectrum should also be considered since they provide independent information on the cosmology (e.g. Mandelbaum *et al.* 2003). However, the Ly $\alpha$  bispectrum as computed from high-resolution QSO spectra is still too noisy to provide significant constraints on the cosmological model (e.g. Viel *et al.* 2004a). To explore a parameter space as large as possible, we will implement a simple semi-analytical model which reproduces many properties of the Ly $\alpha$  absorbers (e.g. Bi, Börner & Chu 1992; Reisenegger & Miralda-Escudé 1995; Bi & Davidsen 1997; Gnedin & Hui 1998). We will generate a wide sample of mock catalogs and constrain the model parameters by comparing their statistical properties to the observations of McDonald *et al.* (2000).

The paper is organized as follows. In Section §2 we briefly review the observational data we aim at fitting in this analysis. In §3.2.1, we detail the method used to compute synthetic spectra from pure dark matter (DM) simulations. The comparison between simulation and observations is done in §4. We discuss our results in §5.

**Table 1.** The main parameters of the  $\Lambda$ CDM simulations considered in the present paper. The normalisation of the RSI simulations follows from the results of Spergel *et al.* (2003). The spectral index  $n_s$  and its derivative  $\mathrm{dln}n_s/\mathrm{dln}k$  are given at  $k = 0.07 \mathrm{hMpc}^{-1}$ . The mass of a dark matter particle is about  $8 \times 10^7 \mathrm{M}_\odot/h$  in all the simulations.

	$\Omega_m$	$\Omega_\Lambda$	$h$	$\sigma_8$	$n_s$	$\mathrm{dln}n_s/\mathrm{dln}k$
S1 and S2	0.30	0.70	0.70	0.90	1	0
R1 and R2	0.31	0.69	0.71	0.84	0.93	-0.03

## 2 OBSERVATIONAL DATA

In this paper, we will compare the simulated statistics to the flux power spectrum and PDF measured by McDonald *et al.* (2000) (hereafter M00), which were obtained from a sample of eight high-resolution QSO spectra. Regarding the flux power spectrum, we consider the data points in the range  $0.005 < k < 0.04 \mathrm{s km}^{-1}$ . The lower limit  $k = 0.005 \mathrm{s km}^{-1}$  is set by the size of our simulations (cf. Section §3.1). Note that it is larger than the characteristic wavenumber  $k \sim 0.003 \mathrm{s km}^{-1}$  below which continuum fitting errors are expected to become important (e.g. Hui *et al.* 2001). The upper limit  $k = 0.05 \mathrm{s km}^{-1}$  is chosen because of concern about metal contamination on smaller scales (e.g. M00; Kim *et al.* 2004). The observed flux PDF is very sensitive to continuum fitting, especially in the high transmissivity tail. We therefore exclude the data points with  $F \geq 0.8$  from the analysis to avoid dealing with continuum fitting error. In addition, we discard also the measurement at  $F = 0$  since it is strongly affected by noise (e.g. Rauch *et al.* 1997). Finally, we emphasize that we work with the power spectrum of the transmitted flux  $F$ ,  $\Delta_F^2(k)$ , which differs from that of the flux density contrast,  $\delta_F \equiv (F/\langle F \rangle - 1)$ , by a multiplicative factor  $\langle F \rangle^2$ .  $\Delta_F^2(k)$  has the advantage that it does not depend explicitly on the mean flux level  $\langle F \rangle$ .

## 3 MODELLING THE Ly $\alpha$ FOREST

In this Section, we will first describe the DM simulations in detail. We will then briefly review the basic ingredients relevant to create realistic Ly $\alpha$  spectra from simulations of DM only.

### 3.1 The N-body simulations

We run DM simulations of a  $\Lambda$ CDM cosmology with the N-body code GADGET (Springel, Yoshida & White 2001). Pure DM simulations are more suitable to our purposes since they allow us to explore a larger parameter space than full hydrodynamical simulations. To reproduce the Ly $\alpha$  forest as seen in QSO spectra and, at the same time, resolve typical absorption systems, a large volume together with a high resolution are requested (e.g. Theuns *et al.* 1998; Bryan *et al.* 1999). For this reason, each simulation evolves  $256^3$  particles of mass  $m \sim 10^8 \mathrm{M}_\odot/h$  in a periodic box of size  $25 \mathrm{h}^{-1} \mathrm{Mpc}$ . Since cosmic variance error on, e.g., the optical depth normalisation (at constant mean flux) can be relatively large

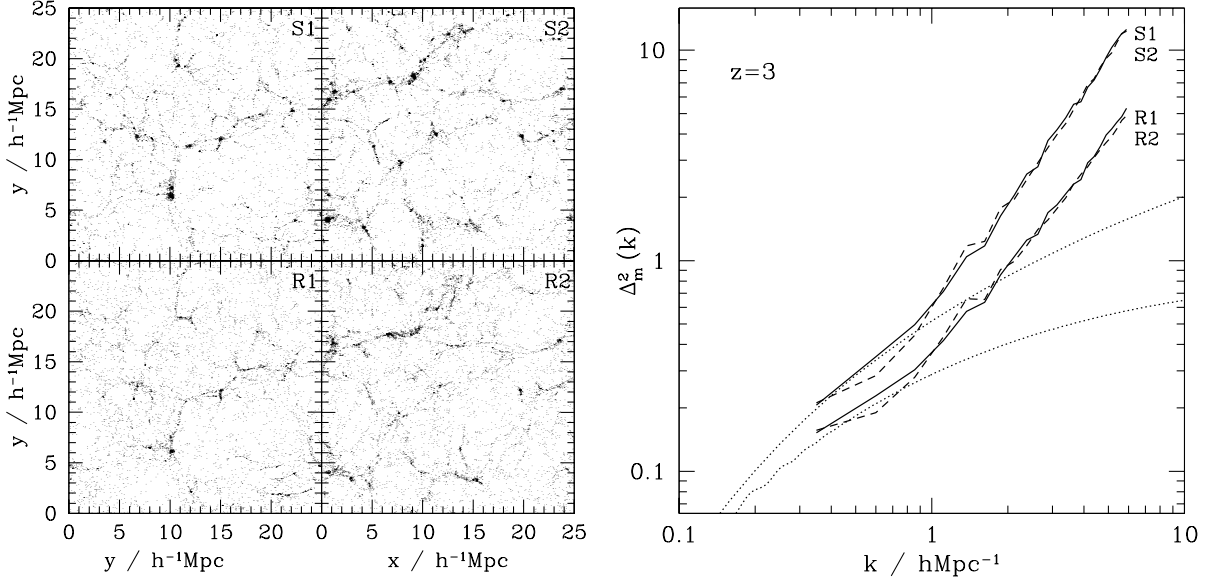


**Figure 1.** *Left panel* : The particle distribution in a slice of thickness  $\Delta h = 0.05 h^{-1}\text{Mpc}$  through the various  $\Lambda\text{CDM}$  simulations at  $z = 3$  : the scale-invariant realisations S1 and S2 (top panels), and the RSI realisations R1 and R2 (bottom panels). *Right panel* : The corresponding 3D power spectra  $\Delta_m^2(k)$  computed at  $z = 3$  from the DM particle distribution. The dashed curves show  $\Delta_m^2(k)$  for the S2 and R2 simulations. The dotted curves show the linear power spectrum used to seed the fluctuations.

when estimated from such a small volume (e.g. Croft *et al.* 2002b), we have run two random realisations of each of the model we consider in the present paper. In the simulations which we denote S1 and S2, the initial power spectrum is scale-invariant,  $n_s = 1$ , and was obtained from fitting formulae of Eisenstein & Hu (1999). In the simulations R1 and R2, the initial power spectrum is that of the running spectral index model (RSI, see e.g. Spergel 2003). The present-day clustering amplitude in these simulations,  $\sigma_8 = 0.84$ , is slightly lower than that of S1 and S2, for which  $\sigma_8 = 0.9$ . The initial particle positions were computed using a parallel code kindly provided by Volker Springel. The cosmological parameters are summarized in Table 1. In the left panel of Fig. 1, we show a slice of thickness  $\Delta h = 0.05 h^{-1}\text{Mpc}$  extracted from the four simulations at redshift  $z = 3$ . Note that the simulations S1 and R1 (S2 and R2) have the same random seed.

To quantify to which extent the various simulations differ, we plot in Fig. 1 the dimensionless 3D matter power spectrum  $\Delta_m^2(k)$  at  $z = 3$  for all the simulations. It was obtained by sampling the DM particles onto a  $512^3$  grid using a cloud-in-cell method, and taking the Fourier transform by means of a FFT routine. As we can see, R1 and R2 exhibit much less power than S1 and S2. On scale  $k \sim 3 h\text{Mpc}^{-1}$ , which corresponds to the pivot point in the flux power spectrum (cf. Figure 4),  $\Delta_m^2(k)$  in the scale-invariant simulations is about twice as large as is in the RSI simulations. Cosmic variance becomes important on scale  $k \lesssim 1 h\text{Mpc}^{-1}$ , where the matter power spectrum computed from the S1 (R1) realisation is larger than that of S2 (R2) by about 10–20%. We also show the linear power spectra which we use to seed fluctuations in the initial DM distribution as dotted curves. The largest scale of the simulations,  $k \lesssim 1 h\text{Mpc}^{-1}$ , are still in the linear regime at  $z = 3$ . Note also that, on

scale  $k \lesssim 0.1 h\text{Mpc}^{-1}$ , the power spectrum of the RSI model is very close to that of the  $n_s = 1$  model.

### 3.2 Generating mock catalogs of QSO spectra

#### 3.2.1 The low density IGM

Semi-analytical models of the Ly $\alpha$  forest exploit the tight relationship between the gas and the underlying DM distribution (e.g. Bi 1993; Bi & Davidsen 1997; Petitjean *et al.* 1995; Gnedin & Hui 1998; Croft *et al.* 1998). In this approach, the gas temperature  $T_g$ , and the neutral hydrogen density  $n_{\text{HI}}$  are computed using tight power-law relations obtained from full hydrodynamical simulations (e.g. Katz *et al.* 1996, Hui & Gnedin 1997, Theuns *et al.* 1998),

$$T_g = \hat{T}_g (1 + \delta_g)^{\gamma-1} \quad \text{and} \quad n_{\text{HI}} = \hat{n}_{\text{HI}} (1 + \delta_g)^\alpha , \quad (1)$$

where the adiabatic index  $\gamma$  is in the range  $1 - 1.62$ , and  $\alpha = 2 - 0.7(\gamma - 1)$ .  $\hat{T}_g$  and  $\hat{n}_{\text{HI}}$  are the temperature and neutral hydrogen density at mean gas density respectively. These scaling relations hold for moderate gas overdensities, i.e.  $\delta_g \lesssim 50^*$ . For higher overdensities however, we have to account for line cooling. To this extent, we follow Desjacques *et al.* (2004) and take the gas temperature to be  $T_g = 10^4 \text{ K}$  for  $\delta\rho/\rho > 50$ . This cutoff ensures that the Doppler parameter  $b(\mathbf{x})$  is always  $b(\mathbf{x}) = 13 \text{ km s}^{-1}$  in the high density regions of the simulation.

When radiative cooling is inefficient, it is reasonable to assume that the gas density and velocity fields,  $\delta_g$  and  $\mathbf{v}_g$ , are smoothed versions of their DM counterparts,  $\delta_m$  and  $\mathbf{v}_m$ . We obtain the gas density distribution by sampling the

\* When pressure smoothing is properly accounted for, this approximation indeed breaks down at much lower overdensities (Schaye 2001)

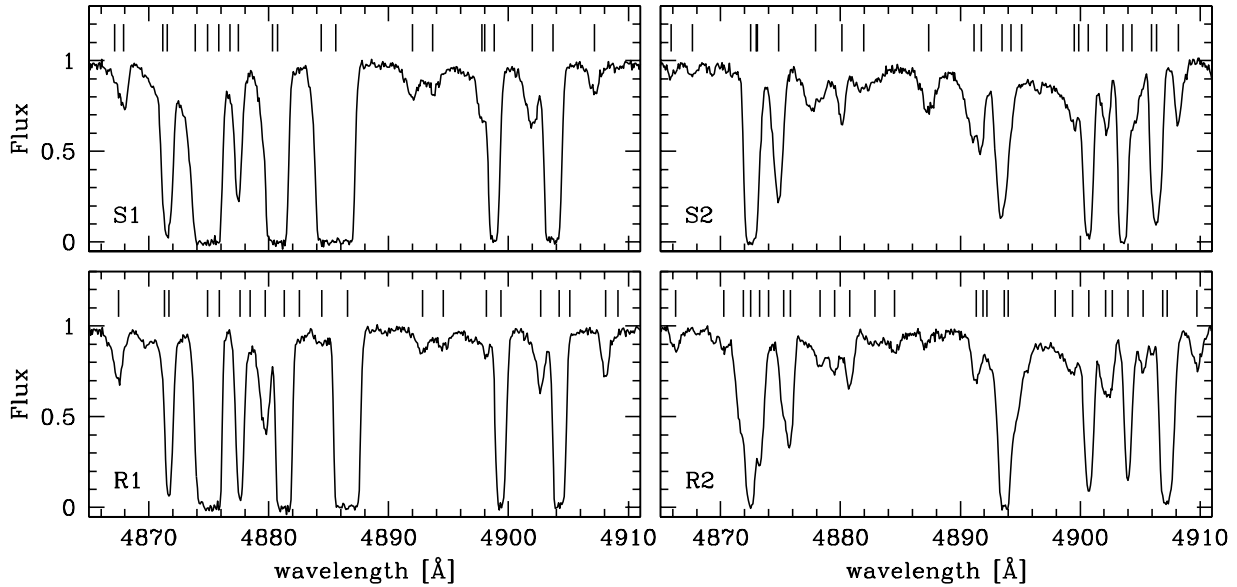


**Figure 2.** Synthetic spectra extracted from each of the simulations at  $z = 3$ . The vertical bars above the spectra show the position of the lines with fitted column densities  $N_{\text{HI}}$  exceeding  $10^{12.5} \text{ cm}^2$ . The comoving length of each spectrum is  $L = 25 h^{-1} \text{ Mpc}$ , and corresponds to a redshift interval  $\Delta z \sim 0.04$  at  $z = 3$ .

DM particles onto a  $512^3$  grid, and smoothing the resulting density field with a Gaussian filter  $W = \exp(-k^2/2k_F^2)$  of characteristic length  $1/k_F$ . This choice is motivated by the fact that a Gaussian filter gives a good fit to the gas fluctuations over a wide range of wavenumber (e.g. Gnedin *et al.* 2003). Furthermore, we expect  $k_F$  to depend on the physical state of the IGM. However, since the relation between  $k_F$  and  $\hat{T}_g$  depends noticeably on the reionization history of the Universe (Gnedin & Hui 1998), it is more convenient to treat  $k_F$  as a free parameter (see e.g. Zaldarriaga, Hui & Tegmark 2001). We discuss gas smoothing in more detail in Appendix §A.

### 3.2.2 The synthetic spectra

Once we have smoothed the DM density and velocity fields on the comoving scale  $1/k_F$ , the flux distribution depends only on the mean flux  $\langle F \rangle$ , the adiabatic index  $\gamma$  and the mean IGM temperature  $\hat{T}_4$ . For any value taken by the four-dimensional parameter vector  $\mathbf{p} = (k_F, \langle F \rangle, \gamma, \hat{T}_4)$ , we generate mock catalogs as follows. For each of the simulations, we randomly select  $10^4$  lines of sight (LOS) of comoving length  $L = 25 h^{-1} \text{ Mpc}$ . The optical depth  $\tau$  and the transmitted flux  $F = \exp(-\tau)$  are then computed along each LOS in 512 pixels of width  $\Delta v \simeq 6 \text{ km s}^{-1}$  according to the Gunn-Peterson approximation (Gunn & Peterson 1965). The resolution of the synthetic spectra is somewhat larger than that of the M00 data, where it is  $\Delta v = 2.5 \text{ km s}^{-1}$ . In order to create realistic Keck spectra, we should have computed the flux on pixels smaller than  $2.5 \text{ km s}^{-1}$ , smooth the spectra with a Gaussian of resolution  $6.6 \text{ km s}^{-1}$  (FWHM), and then resample them on pixels of  $2.5 \text{ km s}^{-1}$ . Unfortunately, FFT of three-dimensional regular grids is still prohibitively slow for meshes larger than  $512^3$ . Notwithstanding, we believe

that the flux power spectrum and PDF will not be much affected. However, we should emphasize that it might not be the case of the line statistics, in particular the line width distribution. In the last step, the value of  $\hat{n}_{\text{HI}}$  is adjusted such that the mean flux  $\langle F \rangle$  of the whole sample matches the desired value (e.g. Rauch *et al.* 1997). To account for the noise in the observations, we add a uniform Gaussian deviate of dispersion  $\sigma = 0.02$  per interval of width  $\Delta \pi = 2.5 \text{ km s}^{-1}$ .

In Fig. 2, we plot four synthetic spectra selected from each of the simulations. The spectra were extracted from mock samples which, for a given simulation, give an acceptable fit to the observed statistics of the Ly $\alpha$  forest (cf. Section §4). In particular, the mean IGM temperature is respectively  $\hat{T}_4 = 1.5$  and  $2$  for the scale-invariant (top panels) and RSI models (bottom panels). Ticks above the spectra mark the Ly $\alpha$  absorption lines which were identified with the spectral fitting program VPFIT (Carswell *et al.* 2003). The lines are distinguished by their column density  $N_{\text{HI}}$  (in  $\text{cm}^{-2}$ ) and their width or Doppler parameter  $b$  (in  $\text{km s}^{-1}$ ). This fitting technique assumes that the fundamental shape of the lines is a Voigt profile, which is a good approximation for column densities  $N_{\text{HI}} \lesssim 10^{17} \text{ cm}^{-2}$  relevant to the Ly $\alpha$  forest. Absorption systems with column density  $N_{\text{HI}} \leq 10^{12.5} \text{ cm}^2$  are quite uncertain and are not shown on the figure (e.g. Bi & Davidsen 1997). The spectra extracted from R1 and R2 feature somewhat more lines than those extracted from S1 and S2. The reason is the larger clustering of the scale-invariant models. As a result, blending of absorbers to form one strong line occurs more often, and cause the number of lines identified with VPFIT to be lower than that in the R1 and R2 models. Note that, in practice, associated metal lines can help fixing the number of subcomponents. We will discuss the properties of the simulated column density distribution in Section §4.4.

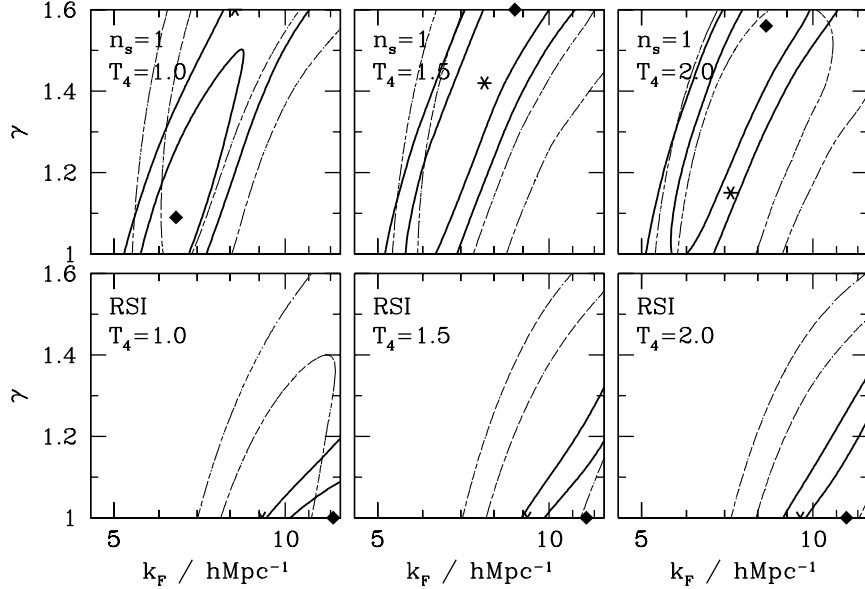


**Figure 3.** Constraints in the plane  $k_F - \gamma$  for a scale-invariant cosmology with  $\sigma_8 = 0.9$  (top panels), and a RSI cosmology (bottom panels). The contours show the 1 and  $2\sigma$  confidence levels (assuming a Gaussian likelihood). The mean IGM temperature is  $\hat{T}_4 = 1$  (left panels), 1.5 (middle panels) and 2 (right panels). The constraint arising from measurements of the flux PS solely is shown as dashed contours, while that arising from the combination of the flux PS and PDF is shown as solid contours. The stars and diamonds mark the best fit models obtained from the PS and PS+PDF data respectively.

#### 4 COMPARISON WITH OBSERVATIONS

In this Section, we compare the statistical properties of our mock catalogs to that of the observations. We perform a  $\chi^2$  statistics for the observed flux power spectrum and PDF. We also compare the simulated line column density and linewidth distributions to observational data for several models.

##### 4.1 The parameter grid

For each value of our parameter vector  $\mathbf{p} = (k_F, \langle F \rangle, \gamma, \hat{T}_4)$ , we generate mock catalogs of ten thousand lines of sight. We let the parameters assume the following values,

$$\begin{aligned} k_F &= 4.55, 5, 5.56, 6.25, 7.14, 8.33, 10, 12.5 \\ \gamma &= 1, 1.1, 1.2, 1.3, 1.4, 1.5, 1.6 \\ \hat{T}_4 &= 0.5, 1, 1.5, 2, 2.5 \\ \langle F \rangle &= 0.60, 0.61, 0.62, \dots, 0.71, 0.72, 0.73 \end{aligned}$$

The values of  $k_F$  (in unit of  $h\text{Mpc}^{-1}$ ) were chosen such that  $1/k_F$  uniformly spans the range  $0.08 - 0.22 h^{-1}\text{Mpc}$ . Our discrete grid thus contains  $8 \times 7 \times 5 \times 14 = 3920$  models. For each mock catalog, we then calculate the flux power spectrum and the flux PDF, and average over the S1 and S2 (resp. R1 and R2) realisations. We then determine the goodness of fit of any model in the grid by computing a  $\chi^2$  statistics from the difference between the simulated PS, PDF and the observational data. We account for measurements of the mean flux  $\langle F \rangle$  by adding a term  $(\langle F \rangle - \bar{F})^2 / \sigma_{\bar{F}}^2$  to the chi-squared, where  $\bar{F}$  and  $\sigma_{\bar{F}}$  are the observed mean flux and error bar at  $z = 3$ . Note that the number of flux PS and PDF measurements used in the analysis is  $10 + 15 = 25$ . Regarding the mean flux level, we will hereafter adopt the

default value of  $M00$ ,  $\bar{F} = 0.684$  and  $\sigma_{\bar{F}} = 0.023$  (see Table 1 of their paper). We should however keep in mind that the presence of metal lines or strong absorption systems can substantially affect the determination of  $\langle F \rangle$  (e.g. Schaye *et al.* 2003; Viel *et al.* 2004b). We will discuss the effect of changing the mean flux level in Section §4.5.

The problem of finding the best fit models is equivalent of finding the maximum of some hypersurface. Since the true maximum does not generally lies exactly at a grid point, it is desirable to interpolate over the different parameters. To this extent, we take advantage of the smooth dependence of the flux PS and PDF on the parameter vector, and use cubic spline interpolation. This method is known to work substantially better than a simple multi-linear interpolation (e.g. Tegmark & Zaldarriaga 2000). To marginalize over a subset of the parameters, we fix their values to that of the best fit model of the subspace, which we obtained from the spline interpolation. To check the accuracy of the interpolation, we computed the flux PS and PDF from the simulations for several randomly selected models which do not lie at a grid point. We found that the flux PS and PDF of the spline-interpolated models differ from that of the 'true' models by  $\lesssim 0.5\%$  only in the range of scales considered in our analysis.

The uniformity of space along the line of sight implies that the different  $k$ -modes of the flux PS are uncorrelated. Uneven sampling of the forest along the line of sight or removal of some regions in the data (such as saturated lines) will introduce covariance between the modes. Yet the covariance matrix of the observed flux power spectrum is reasonably close to diagonal over the scales relevant to our analysis (Croft *et al.* 2002, Viel, Haehnelt & Springel 2004). We will thus neglect correlations between data points in

the flux PS. In the case of the PDF, however, the data points are strongly correlated. As a result, the  $\chi^2$  distribution as computed from the diagonal elements of the error matrix solely might differ noticeably from that computed from the full error matrix (see e.g. M00; Gnedin & Hamilton 2002). The  $\chi^2$  should therefore be computed from the full covariance matrix (available at <http://www.astronomy.ohio-state.edu/jordi/lya>). This covariance matrix reflects the random errors in the flux measurement and, more importantly, the errors resulting from the finite number of QSO spectra. It was estimated using a Monte-Carlo procedure based on a variation of the bootstrap method (Press *et al.* 1992; see Appendix B of M00 for the details). Including the full covariance matrix could have a strong effect on the results, especially when the errors are highly correlated as it is certainly the case in the flux PDF. It is therefore important to assess the sensitivity of our analysis to the details of the covariance matrix. To this purpose, we will initially present results obtained by setting to zero the off-diagonal elements of the covariance matrix. In Section §4.3.3, we will repeat the analysis using the full covariance matrix of the flux PDF, and discuss to which extent the inclusion of the covariance matrix affects the inferred constraints.

Since the spectral fitting program is relatively slow, we have not included the line distribution in the  $\chi^2$  statistics. We will compute the line statistics only for models which best fit the PS and PDF (cf. Section §4.4).

## 4.2 The flux power spectrum and probability distribution

### 4.2.1 Constraint in the $k_F$ - $\gamma$ plane

Fig. 3 shows the constraints in the plane  $k_F$  -  $\gamma$  for the scale-invariant cosmology with  $\sigma_8 = 0.9$  (top panels) and for the RSI cosmology (bottom panels). The mean IGM temperature is  $\hat{T}_4 = 1$  (left panels), 1.5 (middle panels) and 2 (right panels). The contours show the 68.3% and 95.5% confidence levels (assuming a Gaussian distribution for the likelihood) obtained from the flux power spectrum alone (dashed curves), and from a combination of the flux PS and PDF data (solid curves). There is obviously a degeneracy between the filtering wavenumber  $k_F$  and the adiabatic index  $\gamma$ . For illustration, we plot in Fig. 4 the PS and PDF of three scale-invariant models which fit the PS and PDF data at the  $1\sigma$  level. The IGM temperature is  $\hat{T}_4 = 1.5$ . The models are plotted together with the measurements of M00, shown as empty symbols. As we can see, although these models differ in the value of  $k_F$  and  $\gamma$ , they all yield very similar power spectra and PDFs. To understand the origin of this degeneracy, note that increasing  $\gamma$  generally reduces the width of the weak lines ( $\tau \lesssim 1$ ) relative to that of the strong lines ( $\tau \gtrsim 1$ ). This follows from the fact that the low column density Ly $\alpha$  forest arises in gas of low overdensity. Consequently, increasing  $\gamma$  (at constant mean flux) amounts to decreasing  $\Delta_F^2(k)$  on small scale, and thereby mimics the effect of a smaller  $k_F$ . In the PDF, increasing  $\gamma$  enhances the fraction of transmissivity pixels in the range  $F \gtrsim 0.5$  presumably because, at constant mean flux, the lower optical depth normalisation and the reduction in the width of the weak lines conspire to increase the fraction of high transmissivity pixels. As a result, the combination of the PS and PDF cannot break

the degeneracy since both statistics exhibit a similar dependence on  $k_F$  and  $\gamma$ . In reality however, one would expect the filtering length to depend on  $\hat{T}_g$  and  $\gamma$  (see Appendix §A). Therefore, additional assumptions on the reionization history of the Universe could break this degeneracy. In this respect, the observed line-width distribution suggests that, around  $z = 3$ , there is a sharp increase in  $\hat{T}_g$  together with a decrease in  $\gamma$  (Schaye *et al.* 2000; Ricotti, Gnedin & Shull 2000; see however McDonald *et al.* 2001). However, the data are too noisy to constrain  $\hat{T}_4$  and  $\gamma$  significantly.

### 4.2.2 The best fit models

In Fig. 3, the stars and squares symbols mark the models which best fit the PS and PS+PDF data, respectively. These models are compared in Fig. 5 to the M00 data. The temperature of the scale-invariant models was chosen to be  $\hat{T}_4 = 1.5$ , while the RSI models have  $\hat{T}_4 = 2$ . This choice is motivated by the fact that, in a scale-invariant cosmology with  $\sigma_8 = 0.9$ , models with  $\hat{T}_4 \lesssim 1.5$  fit the data best whereas, in a RSI cosmology, the best fit are obtained for  $\hat{T}_4 \gtrsim 2$  (cf. Table 2). The RSI models match the observed  $\Delta_F^2(k)$  somewhat better than the scale-invariant models. However, they tend to overestimate the PDF in the range  $F \gtrsim 0.6$ , which roughly traces regions of gas overdensity  $\delta_g \lesssim 0$ . This follows from the relative lack of small-scale power, which translates into larger values of the PDF in the high transmissivity tail. Consequently, matching the flux PDF in a RSI cosmology requires a low filtering length. Indeed, although the RSI models which best fit the PS data alone have  $k_F \lesssim 10 \text{ hMpc}^{-1}$ , those which best fit the PS+PDF data have  $k_F \gtrsim 11 \text{ hMpc}^{-1}$ , close to the largest value assumed by  $k_F$  in our parameter grid. Since the Nyquist frequency of the grid is  $k_{Ny} \approx 10.2 \text{ hMpc}^{-1}$ , these models are certainly affected by numerical resolution. However, numerical resolution also contributes to the smoothing (e.g. Zaldarriaga, Hui & Tegmark 2001), and  $k_F = 11 \text{ hMpc}^{-1}$  is merely a lower limit. Note that we have  $k_F \sim 6 - 9 \text{ hMpc}^{-1}$  for the best scale-invariants models, a filtering scale which is robust to resolution issues.

Fig. 5 also clearly demonstrates that models which match best the PS data alone do not yield a good fit of the PDF. The constraints inferred from measurements of  $\Delta_F^2(k)$  alone might thus be significantly biased. It is therefore important to combine the PS and PDF statistics to ensure that both are correctly reproduced in the simulation. To quantify the effect of adding the PDF, we plot in Fig. 6 the flux power spectrum and PDF of scale-invariant models for several values of  $\hat{T}_g$ . Models which fit best the PS and the PS+PDF data are shown in the top and bottom panels, respectively. When the PS data alone are fitted, the agreement between the observed and simulated flux PDF worsens with increasing temperature. For  $\hat{T}_4 \gtrsim 2$ , the disagreement is very severe. A comparison between the top and bottom left panels reveals that including the PDF in the  $\chi^2$  statistics increases the amplitude of flux power spectrum by an amount of  $\sim 10\%$  on scale  $k \lesssim 0.01 \text{ skm}^{-1}$ . Increasing the temperature produces a similar but weaker effect : the large-scale amplitude of  $\Delta_F^2(k)$  decreases by about 5% when the temperature increases from  $\hat{T}_4 = 1$  to 2. Note that the strength of this effect is consistent with findings from

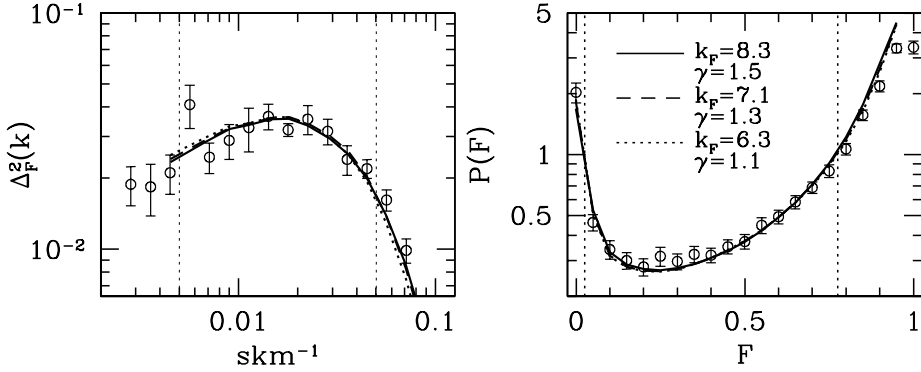


**Figure 4.** Three scale-invariant models of normalisation  $\sigma_8 = 0.9$  which give an acceptable fit to the observed flux PS and PDF. The mean IGM temperature is  $\hat{T}_4 = 1.5$ . The reduced chi-squared are  $\chi^2 = 23.5, 23.2$  and  $22.8$  (for 23 degrees of freedom) for  $\gamma = 1.5, 1.3$  and  $1.1$  respectively. Only the data points which lie between the two vertical lines were used to compute the  $\chi^2$  statistics.

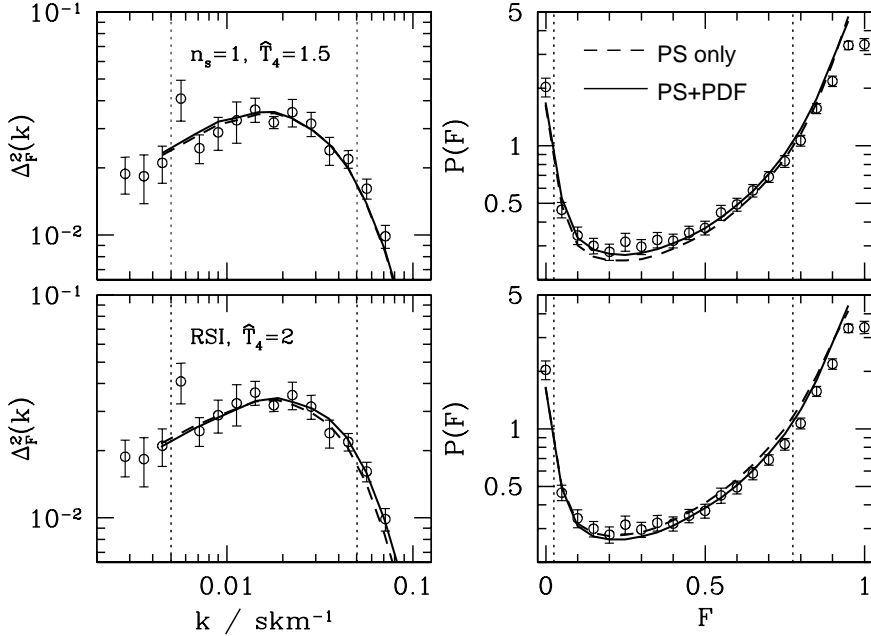


**Figure 5.** A comparison between models which best fit the PS data alone (dashed curves), and models which best fit the PS+PDF data (solid curves). They are shown for the  $\sigma_8 = 0.9$ , scale-invariant cosmology (top panels), and for the RSI cosmology (bottom panels), for a fixed temperature  $\hat{T}_4 = 1.5$  and  $2$  respectively. For the PS data only, the best fit values of the other parameters are  $(k_F, \langle F \rangle, \gamma) = (7.7, 0.71, 1.42)$  and  $(9.5, 0.69, 1)$  in the  $n_s = 1$  and RSI models respectively, whereas with the PS+PDF data, they are  $(8.7, 0.69, 1.6)$  and  $(11.5, 0.70, 1)$ .

hydrodynamical simulations (e.g. Viel, Haehnelt & Springel 2004). Combining the PS and PDF data could therefore reduce the best fit value of  $\sigma_8$  by about 10%. We also expect a degeneracy between the  $\sigma_8$  and the mean IGM temperature. The data could be equally matched with a lower  $\sigma_8$  and a larger IGM temperature. We will discuss this issue in more detail in Section §4.3.

The photoionisation rate  $\Gamma_{-12}$  of the neutral hydrogen (in unit of  $10^{-12} \text{ s}^{-1}$ ) can be estimated from the optical depth normalisation  $\tau_0$ , which can be written as

$$\tau_0 = 2.31 \mathcal{A}(z) \hat{T}_4^{-0.7} \left( \frac{1+z}{4} \right)^6, \quad (2)$$

where  $\mathcal{A}(z) = (\Omega_b h^2 / 0.02)^2 H_{100}(z)^{-1} \Gamma_{-12}(z)^{-1}$ . Here,  $\Omega_b$  is the baryon content and  $H(z)$  the Hubble constant in unit of  $100 \text{ km s}^{-1} \text{ Mpc}^{-1}$  (e.g. Rauch *et al.* 1997; McDonald *et al.* 2000). To calculate  $\Gamma_{-12}$ , we assume  $\Omega_b h^2 = 0.02$ , in agreement with the constraint derived from CMB and deuterium abundance measurements (e.g. Spergel *et al.* 2003; Burles & Tytler 1998). For the models of Fig. 5 which best fit the PS+PDF data, the optical depth normalisation is

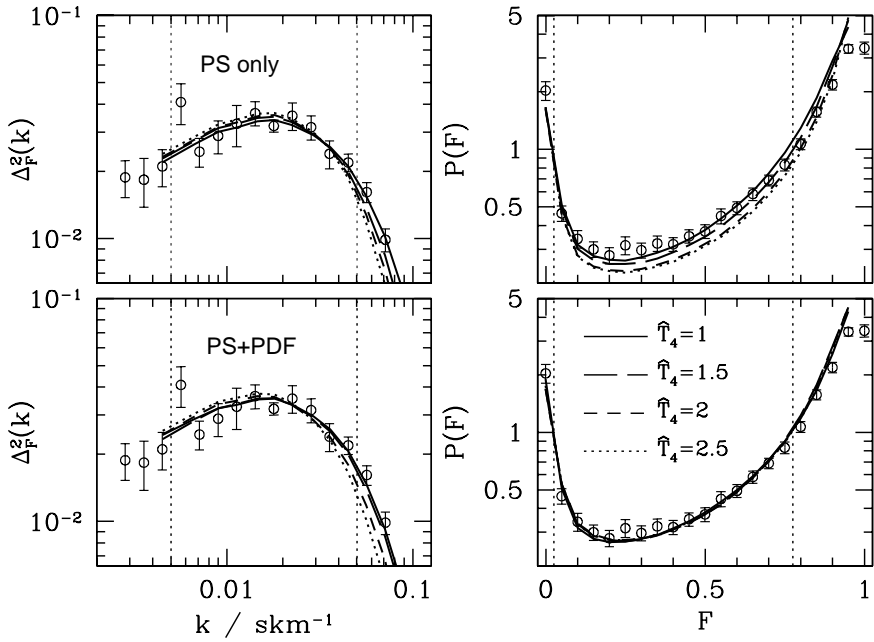


**Figure 6.** Scale-invariant models of rms fluctuation  $\sigma_8 = 0.9$  which fit best the PS data solely (top panels), and the PS+PDF data (bottom panels) as a function of the mean IGM temperature. The temperature has a fixed  $\hat{T}_4 = 1$  (solid), 1.5 (long-dashed), 2 (short-dashed) and 2.5 (dotted curves), while the other parameters were varied. The best fit parameter values obtained with the PS+PDF data are listed in Table 2.

**Table 2.** Parameter values of scale-invariant and RSI models which best fit the PS+PDF data, for a mean IGM temperature  $\hat{T}_4 = 1, 1.5, 2$  and  $2.5$ . The filtering  $k_F$  is in unit of  $h\text{Mpc}^{-1}$ . The last column gives the chi-squared for 23 degrees of freedom. Note that, since we spline interpolate over the parameters, the best fit values do not necessarily lie at a grid point.

model	$\hat{T}_4$	$\langle F \rangle$	$k_F$	$\gamma$	$\chi^2$
$n_s = 1, \sigma_8 = 0.72$	1	0.69	7.2	1	21.4
	1.5	0.70	11.1	1.6	18.9
	2	0.70	10.2	1.53	21.0
	2.5	0.70	8.8	1.37	24.9
$n_s = 1, \sigma_8 = 0.82$	1	0.69	6.6	1	20.9
	1.5	0.69	9.7	1.6	21.4
	2	0.70	9.1	1.55	25.1
	2.5	0.70	8.1	1.42	30.4
$n_s = 1, \sigma_8 = 0.9$	1	0.69	6.5	1.16	21.3
	1.5	0.69	8.8	1.6	23.7
	2	0.69	8.2	1.55	28.4
	2.5	0.69	7.7	1.45	34.9
$n_s = 1, \sigma_8 = 1$	1	0.68	6.9	1.29	21.3
	1.5	0.69	8.0	1.57	25.4
	2	0.69	7.9	1.56	32.0
	2.5	0.69	7.0	1.42	39.9
RSI	1	0.7	12.1	1	31.3
	1.5	0.7	11.6	1	25.7
	2	0.7	11.5	1	22.2
	2.5	0.7	12.5	1.07	20.6

$\tau_0 \sim 0.9$  (scale-invariant) and  $\sim 0.8$  (RSI). The inferred photoionisation rate for both best fit models is  $\Gamma_{-12} \sim 0.6$ , a value consistent with other estimates (e.g. Rauch *et al.* 1997; McDonald & Miralda-Escudé 2001). Note, however, that this does not ensure that our simulations fully resolve the Ly $\alpha$  forest (cf. Section §3.2.2).

### 4.3 Sensitivity to the clustering amplitude

As we discussed before, a scale-invariant model with a clustering amplitude of  $\sigma_8 = 0.9$  matches best the data when the IGM temperature is low. Nonetheless, we could improve the agreement with the data in the range  $\hat{T}_4 \gtrsim 1.5$  by decreasing the rms density fluctuations. To assess the sensitivity of the statistics to  $\sigma_8$ , we take advantage of the self-similarity of gravitational clustering in EdS cosmology (a good approximation at redshift  $z \gtrsim 2$ ). As a result, a snapshot at redshift different from  $z = 3$ , once rescaled, can mimic a cosmology with a different  $\sigma_8$ . Since the fluctuation amplitude of the RSI model is tightly constrained by the CMB and Ly $\alpha$  forest data (e.g. Bennett *et al.* 2003; Spergel *et al.* 2003), we will vary  $\sigma_8$  in the scale-invariant cosmology only. We consider snapshots separated by a redshift interval  $\Delta z = 0.2$  in the range  $z = 2 - 4$ . These snapshots thus mimic scale-invariant cosmologies of rms density fluctuation  $0.7 \lesssim \sigma_8 \lesssim 1.1$ .

#### 4.3.1 Correlation between $\sigma_8$ and $\hat{T}_g$

In Fig. 7, we compare the PS (top panel) and the PDF (bottom panel) of several best fit models with different clustering amplitudes :  $\sigma_8 = 0.72$  (solid), 0.82 (long-dashed), 0.9 (short

dashed) and 1 (dashed-dotted curves). We also show the best fit RSI model as a dotted curve. The mean IGM temperature was chosen to be  $\hat{T}_4 = 1.5$ . For sake of completeness however, we list in Table 2 the parameters values of best fit models for a mean IGM temperature in the range  $1 \leq \hat{T}_g \leq 2.5$ . A comparison between the scale-invariant  $\sigma_8 = 0.82$  model and the RSI which has a very similar  $\sigma_8$ , demonstrates that the best fit power spectrum on scale  $k \lesssim 0.01 \text{ s km}^{-1}$  is very sensitive to the small-scale behaviour of the matter power spectrum. Indeed, the difference in the flux power spectrum of these two models mainly results from including the PDF in the chi-squared statistics. This illustrates the advantage of combining several statistics of the Ly $\alpha$  forest in constraining the shape of the linear power spectrum.

The scale-invariant models fit the flux power spectrum and the PDF reasonably well. However, the large-scale amplitude of their flux PS increases with  $\sigma_8$ , and causes the models with  $\sigma_8 \gtrsim 0.9$  to overestimate the data on scale  $k \lesssim 0.01 \text{ s km}^{-1}$ . To assess the significance of this effect, we need an estimate for the cosmic variance error in the flux PS. To this purpose, we ran two additional simulations (S3 and S4) of a scale-invariant cosmology with normalisation  $\sigma_8 = 0.9$  and computed the flux PS and PDF for the best fit models of Fig. 7. Then, from the sample of simulations  $S1 \rightarrow S4$ , we computed the flux PS and PDF for the six possible combinations of two simulations. The cosmic variance error was then the  $1\sigma$  scatter around the mean. For clarity, we use an offset and plot in Fig. 7 the cosmic variance as errorbars in the bottom of each panel. The errorbars are shown for the model with  $\sigma_8 = 0.9$  only, as we found that they do not change much among the models. As we can see, they are small, about  $\lesssim 3\%$  and  $\lesssim 2\%$  in the flux PS and PDF respectively. However, since our simulations lack of large-scale power, they most probably underestimate the true cosmic variance. Yet the flux PS of the models with  $\sigma_8 \gtrsim 0.9$  would still confidently lie above the data points on scale  $k \lesssim 0.01 \text{ s km}^{-1}$ , even if the errors were twice as large. This demonstrates that, at fixed temperature,  $\Delta_F^2(k)$  increases with  $\sigma_8$  on scale  $k \lesssim 0.01 \text{ s km}^{-1}$ . Consequently, there is a degeneracy between the temperature and  $\sigma_8$ . A model with larger  $\sigma_8$  requires a lower temperature to match the observed flux power spectrum. Note, however, that the measurement errors are large in that range of wavenumber. As a result, although the models with  $\sigma_8 \gtrsim 0.9$  shown in Fig. 7 predict a flux power spectrum which, “by eye”, overestimates the observations, they are still consistent with the data in a  $\chi^2$  sense at least (The worst chi-squared,  $\chi^2 = 25.4$  for 23 degrees of freedom, is obtained for  $\sigma_8 = 1$ , and corresponds to a fit probability  $\sim 30\%$ ).

To illustrate the correlation between the mean IGM temperature and  $\sigma_8$ , we plot in Fig. 8 the difference  $\Delta\chi^2 = \chi^2 - \chi^2_{\min}$  as a function of  $\sigma_8$ , after marginalizing over the mean flux level  $\langle F \rangle$ . The other parameters do not vary in the chi-squared minimization. The mean IGM temperature is  $\hat{T}_g = 1$  (left panel), 1.5 (middle panel) and 2 (right panel), the filtering is  $k_F = 8.3$  (solid curve), 7.1 (long-dashed) and  $6.3 \text{ hMpc}^{-1}$  (short-dashed), and the adiabatic index has a fixed value  $\gamma = 1.3$ . These values of  $\hat{T}_g$  and  $\gamma$  are consistent with that inferred from observations at  $z \sim 3$  (e.g. Schaye *et al.* 2000; Ricotti, Gnedin & Shull 2000; McDonald *et al.* 2001). The reason for selecting particular values of  $\gamma$  and  $k_F$

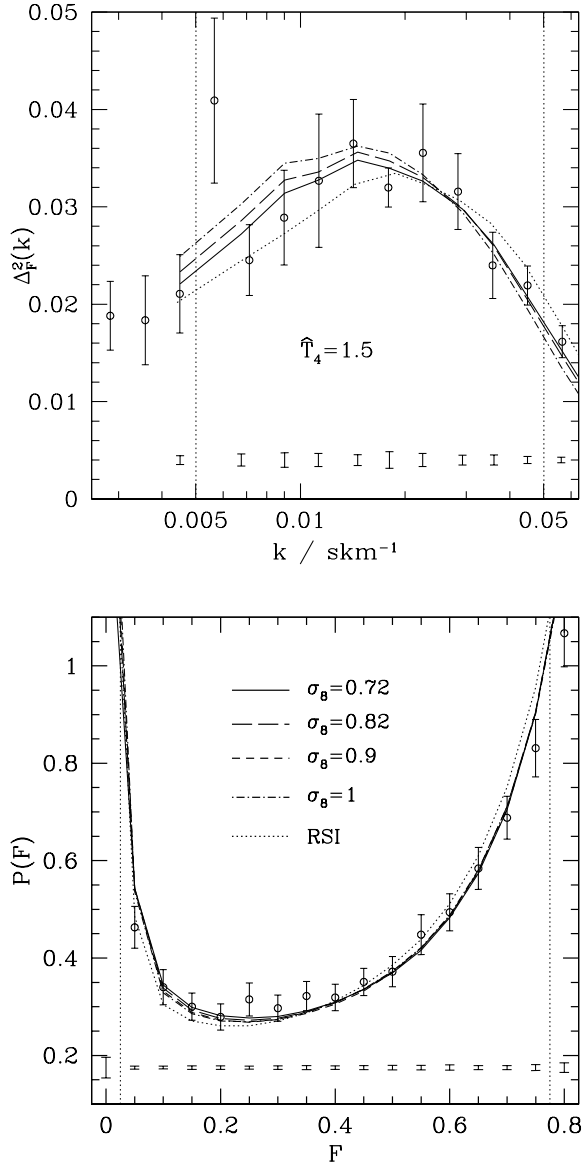


**Figure 7.** A comparison between the flux PS (top panel) and PDF (bottom panel) of scale-invariant models with rms density fluctuation  $\sigma_8 = 0.72$  (solid), 0.82 (long-dashed), 0.9 (short dashed) and 1 (dashed-dotted curve). The RSI model is shown as dotted curves. The IGM temperature has a fixed value  $\hat{T}_4 = 1.5$ , while the other parameters are varied to obtain the best agreement with the data. The best fit models are listed in Table 2. In the bottom of each panel, the errorbars show our estimate of the cosmic variance for the model with  $\sigma_8 = 0.9$  (cf. text).

follows from the fact that marginalizing over these parameters proves difficult because of their degeneracy. The large measurement errors worsen the situation. However, we can take advantage of the fact that the subspace  $k_F \gamma$  has one effective degree of freedom. Namely, we can fix the adiabatic index  $\gamma$  and select several values of the filtering length  $k_F$  without restricting the analysis. Note that the wiggles which appear in  $\Delta\chi^2$  are caused by numerical instabilities in the spline interpolation. Fig. 8 demonstrates that, at a given filtering  $k_F$ , decreasing the temperature increases the nor-

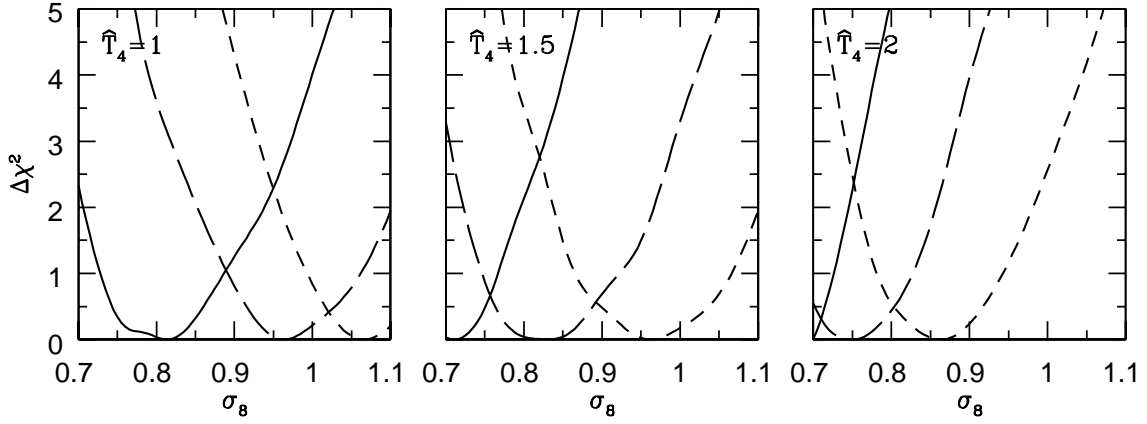


**Figure 8.** Constraint on  $\sigma_8$  from a fit to the observed flux PS and PDF after marginalization over the the mean transmitted flux. Only the parameters  $\sigma_8$  and  $\langle F \rangle$  were varied. The curves show  $\Delta\chi^2 = \chi^2 - \chi^2_{\min}$  for a mean IGM temperature  $\hat{T}_4 = 1$  (left panel), 1.5 (middle panel) and 2 (right panel). The filtering is  $k_F = 8.3$  (solid curve), 7.1 (long-dashed) and  $6.3 \text{ hMpc}^{-1}$  (short-dashed). The adiabatic index has a fixed value  $\gamma = 1.3$ .

malisation  $\sigma_8$  of the best fit models ( $\Delta\chi^2 = 0$ ). Moreover, at fixed temperature, decreasing the filtering  $k_F$  also increases the best fit  $\sigma_8$ . For e.g.  $\hat{T}_4 = 1.5$ , we find  $\sigma_8 \approx 0.71, 0.83$  and  $0.96$  for  $k_F = 8.3, 7.1$  and  $6.3 \text{ hMpc}^{-1}$ . In other words, one has to increase the clustering amplitude in order to compensate for the larger smoothing. It would therefore be possible to match the data with a normalisation  $\sigma_8 \gtrsim 1$  if both the filtering and the IGM temperature were very low,  $k_F \approx 6 \text{ hMpc}^{-1}$  and  $\hat{T}_4 \approx 1$ . Indeed, a model where  $k_F = 6.3 \text{ hMpc}^{-1}$  and  $\hat{T}_4 = 1$  has a best fit value  $\sigma_8 = 1.06$ , and fits the data with an acceptable chi-squared  $\chi^2 = 22.4$  for 24 degrees of freedom.

#### 4.3.2 A temperature-dependent filtering

As we discussed in the previous Section, a model with  $\sigma_8 \gtrsim 1$  can match the data if both  $T_g$  and  $k_F$  are very low. In reality, however, these two parameters are not independent since the filtering  $k_F$  to increase with the temperature (when all the other parameters are fixed). To make further progress, we will assume that the filtering  $k_F$  is solely a function of the mean IGM temperature  $\hat{T}_g$ . In Appendix §A, the dependence of  $k_F$  on the IGM temperature and the reionization history of the Universe is discussed in detail. In brief, we expect the filtering scale to decrease with increasing temperature as  $k_F \propto \hat{T}_4^{-1/2}$ , and to be smaller than  $\sim 14 \text{ hMpc}^{-1}$  at  $z = 3$  for reasonable reionization scenarios (cf. Appendix §A).

To assess the effect of such an assumption on the constraint inferred from the flux PS and PDF, we plot in the left panel of Fig. 9  $\Delta\chi^2$  as a function of  $\sigma_8$  after marginalizing over the mean flux. Only  $\sigma_8$  and  $\langle F \rangle$  were varied to obtain the flux PS and PDF of the best fit models shown in the right panel. We assumed a temperature-dependent filtering scaling as  $k_F = 10\hat{T}_4^{-1/2}$  (curves with triangles) and  $8\hat{T}_4^{-1/2} \text{ hMpc}^{-1}$  (curves with squares). The results are shown for different values of the temperature,  $\hat{T}_4 = 1$  (solid curves), 1.5 (long-dashed) and 2 (short-dashed), but for a fixed value of the adiabatic index,  $\gamma = 1.3$ . The param-

eter values of the best fit models are listed in the upper half of Table 3. The temperature-dependent filtering causes the best fit value of  $\sigma_8$  to increase with the temperature. The rms fluctuations even reaches  $0.9 - 0.95$  for a filtering  $k_F = 10\hat{T}_4^{-1/2}$  and a temperature  $\hat{T}_4 \lesssim 1.5$ . Most importantly, the amount of filtering significantly matters, as the best fit parameters are rather sensitive to the normalisation of the relation  $k_F(\hat{T}_4)$ . At fixed temperature, a scaling  $k_F = 8\hat{T}_4^{-1/2}$  leads to best fit values of  $\sigma_8$  which are 10-20% larger than a scaling  $k_F = 10\hat{T}_4^{-1/2}$ . This strongly suggests that the Gaussian filter approximation (e.g. Gnedin *et al.* 2003) is certainly not accurate enough to constrain the clustering amplitude to better than  $\sim 10\%$ . A close look at the right panel of Fig. 9 also reveals that the models with  $k_F(1) = 10 \text{ hMpc}^{-1}$  <sup>†</sup> look consistent with the data, whereas those with  $k_F(1) = 8 \text{ hMpc}^{-1}$  tend to overestimate  $\Delta_F^2(k)$  on scale  $k \lesssim 0.01 \text{ s km}^{-1}$ , especially when the temperature is large,  $\hat{T}_4 \gtrsim 1.5$ . The best fit values of the clustering amplitude inferred from a temperature-dependent filtering  $k_F \leq 10\hat{T}_g^{-1/2}$  are  $\sigma \gtrsim 0.7$ . However, since the Nyquist frequency of the grid is  $k_{\text{Ny}} \approx 10.2 \text{ hMpc}^{-1}$ , we cannot robustly probe the range of wavenumber  $k_F(1) \gtrsim 10 \text{ hMpc}^{-1}$ . Consequently, our analysis cannot exclude values of  $\sigma_8$  as low as  $\sigma_8 \leq 0.7$ . However, since  $k_F(1) = 14 \text{ hMpc}^{-1}$  is probably an unrealistically high value for the filtering wavenumber at redshift  $z = 3$  (Appendix §A), we expect  $0.7 \lesssim \sigma_8 \lesssim 0.9$  from the present results for a reasonable choice of reionization history, and an IGM temperature in the range  $1 \lesssim \hat{T}_4 \lesssim 2$ .

#### 4.3.3 Effect of including the full PDF error matrix

As yet we have set to zero all the off-diagonal elements of the error matrix. We now present results with the full error covariance matrix as given in McDonald *et al.* (2001). A comparison between the results in the two cases allows

<sup>†</sup>  $k_F(1)$  stands for  $k_F(\hat{T}_4 = 1)$ .

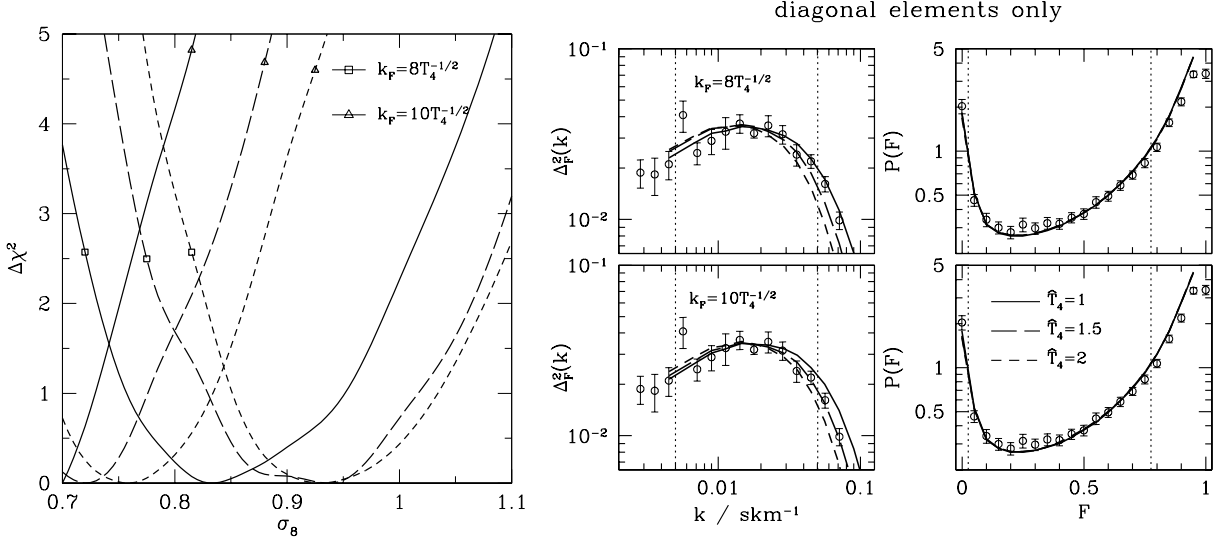


**Figure 9.** *Left panel* :  $\Delta\chi^2$  after marginalizing over the mean flux level. Only  $\sigma_8$  and  $\langle F \rangle$  were varied to obtain the best fit parameters. The mean IGM temperature  $\hat{T}_4 = 1$  (solid curves), 1.5 (long-dashed) and 2 (short-dashed). The filtering scales with  $\hat{T}_4$  as  $k_F = 8\hat{T}_4^{-1/2}$  (curves with squares) and  $10\hat{T}_4^{-1/2} \text{ hMpc}^{-1}$  (curves with triangles). The adiabatic index has a fixed value  $\gamma = 1.3$ . The spline interpolation was performed using the diagonal elements of the PDF covariance matrix solely. *Right panel* : The flux power spectrum and PDF of the best fit models ( $\Delta\chi^2 = 0$ ). The IGM temperature is  $\hat{T}_4 = 1$  (solid curves), 1.5 (long-dashed) and 2 (short-dashed), for a fixed adiabatic index  $\gamma = 1.3$ . The best fit values of  $\sigma_8$ ,  $\langle F \rangle$  together with the chi-squared are listed in the upper half of Table 3.

an assessment of the robustness of the inferred best fit parameters. Since we are interested in the measurements with  $0.05 \leq F \leq 0.75$ , we obtain the desired covariance matrix by setting the errors of the data points outside that range to infinity. Curves of  $\Delta\chi^2$  versus  $\sigma_8$  are plotted in the left of Fig. 10. In the panel to the right of the same figure flux power spectra and PDFs corresponding to the best fit parameters are shown. Values of the best fit parameters are listed in the lower half of Table 3. Taking into account the covariance matrix of the flux PDF in the chi-squared minimization introduces a systematic shift in the central values of the best fit parameters. Yet the effect is rather small. The clustering amplitude,  $\sigma_8$ , gets lower by only a few percents in most cases. The wiggles in the chi-squared curves in the left panel of Fig. 10 lead to a highly non-gaussian distribution for the statistical errors on the best fit parameters. As a result, assessing to which extent the errors on the best fit values of  $\sigma_8$  compare with those inferred from the diagonal elements only proves difficult. However, we found that at fixed  $\sigma_8$  and  $\hat{T}_g$ , including the off-diagonal elements increases the confidence levels in the plane  $k_F - \gamma$  by 5–10% (cf. Section §4.2.1). Finally, a comparison between the right panels of Fig. 9 and 10 reveals that, when the full covariance matrix is included, the flux PDF of the best fit models falls systematically below the data points in the range  $0 \lesssim F \lesssim 0.5$ . This kind of behaviour is likely to occur when the errors are strongly correlated, as it is the case for the flux PDF. The curve for which the likelihood is the largest is not necessarily the one which goes through the error bars attached to the data points.

#### 4.4 The observed line statistics

To assess whether the best fit models reproduce the observed line statistics, we compute the column density and line width distributions, and compare our results to observational data.

##### 4.4.1 The column density distribution

The differential line density distribution  $f(N_{\text{HI}})$  is defined as the number of lines per unit column density and per unit absorption distance (see e.g. Tytler 1987; Schaye 2001), which is  $dX/dz \approx \Omega_m^{-1/2}(1+z)^{1/2}$  at redshift  $z \sim 3$  in the standard  $\Lambda$ CDM model. However, to facilitate the comparison with the measurements of Petitjean *et al.* (1993) and Hu *et al.* (1995), who assumed a deceleration parameter  $q_0 = 0$ , we take the absorption distance to be  $dX/dz = (1+z)$ . In the left panel of Fig. 11 we plot the column density distribution for several models which give a good fit of the PS and PDF data ( $\chi^2/\nu \lesssim 1$ ).  $f(N_{\text{HI}})$  was calculated from a sample of 40 LOS. The simulated curves are compared to the data of Hu *et al.* (1995) and Petitjean *et al.* (1993), which are shown as filled circles and squares respectively. The mean redshift of both samples is  $z = 2.8$ , close to that of the M00 data considered in the present paper. We plot  $f(N_{\text{HI}})$  for two scale-invariant,  $\sigma_8 = 0.9$  models with different values of  $k_F$  and  $\gamma$  :  $(k_F, \gamma) = (8.3, 1.5)$  (solid curve) and  $(6.3, 1.1)$  (solid-dotted curve). In addition, we show  $f(N_{\text{HI}})$  for a cold ( $\hat{T}_4 = 1.5$ ) and a hot ( $\hat{T}_4 = 2.5$ ) scale-invariant model of normalisation  $\sigma_8 = 0.72$  as long- and short-dashed curves respectively. The RSI model is shown as a dotted curve. Absorption lines with column density  $10^{12.5} \leq N_{\text{HI}} \leq 10^{15.5} \text{ cm}^{-2}$  contribute most to the Ly $\alpha$  forest. In that range, the simulated column density distributions agree very well with the data. In particular, the slope and the normalisation of the simulated distributions coincides with that of the observations. The

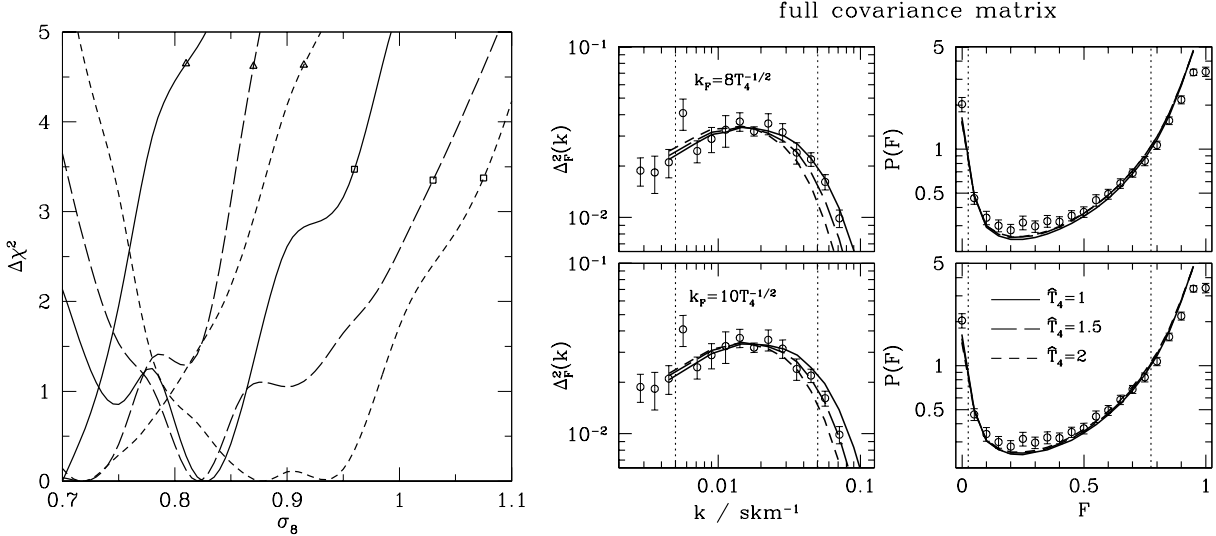


**Figure 10.** Same as Fig. 9. However, the full covariance matrix of the flux PDF (cf. text) was used instead of the diagonal elements only. The best fit parameter values are listed in the lower half of Table 3.

later also tends to steepen in the range  $N_{\text{HI}} \gtrsim 10^{14} \text{ cm}^{-2}$ . Such a deviation from a single power law is also found in the observations (e.g. Petitjean *et al.* 1993; Kim *et al.* 1997). Fig. 11 demonstrates that, although the flux PS and PDF of the best fit models is rather sensitive to the normalisation amplitude and the relative amount of small-scale power (cf. Section §4.3), the column density distribution barely changes among the various models, in agreement with the results of Theuns, Schaye & Haehnelt (2000) who found that  $f(N_{\text{HI}})$  is insensitive to the amount of small scale power. If most of the lines identified by VPFIT have a column density  $N_{\text{HI}} \lesssim 10^{15.5} \text{ cm}^{-2}$  ( $\sim 10^3$  for a sample of 40 LOS), absorption systems with column density exceeding  $N_{\text{HI}} \gtrsim 10^{15.5}$  are rare ( $\lesssim 30$ ). It is however crucial to reproduce them since they can contribute up to 50% of the flux power spectrum on scale  $k \lesssim 0.01 \text{ s km}^{-1}$  (e.g. Viel *et al.* 2004b). Although the column density distribution suffers from the shot noise associated to these rare events, the left panel of Fig. 11 shows clearly that our simulations reproduce, at least qualitatively, these strong absorption systems.

#### 4.4.2 The line-width distribution

The line-width distribution,  $f(b)$ , which is the fraction of line with a given width, is shown in the right panel of Fig. 11 for the models plotted in the left panel.  $f(b)$  is computed from absorption systems with column density  $10^{12.5} - 10^{14.5} \text{ cm}^{-2}$ . The solid histogram is the data of Hu *et al.* (1995). The observed line-width distribution clearly exhibits a peak in the range  $b \sim 20 - 40 \text{ km s}^{-1}$ . In this respect, Fig. 11 shows that in the simulations, the peak is more pronounced for a model with larger value of  $\gamma$  at constant  $\sigma_8$ . Furthermore, the scale-invariant model with lower normalisation ( $\sigma_8 = 0.72$ ) and the RSI model account somewhat better for the amplitude of the observed peak,  $f(b) \sim 0.04$ . However, given the large measurement errors, using  $f(b)$  to constrain the parameter of the model does not seem feasible. Most importantly, it has been demonstrated that very high-resolution hydro-

simulations are needed to reliably predict  $f(b)$  (Theuns *et al.* 1998; Bryan *et al.* 1999; Theuns, Schaye & Haehnelt 2000). Consequently, it is difficult to draw any firm conclusion on the sensitivity of the line-width distribution to the shape and amplitude of the matter power spectrum of the best fit models.

#### 4.5 Systematic errors

Various sources of error affect our analysis, among them systematics in the data and in the modelling of the Ly $\alpha$  forest. Regarding the data, note that the M00 measurements, obtained from a sample of 8 QSO only, are quite noisy. In the flux power spectrum for example, the data point at  $k = 0.00566 \text{ s km}^{-1}$  lies well above the others. One might be worried that our results are strongly affected by this single data point. However, the corresponding error,  $\sim 20\%$ , is larger than that of the other data points. For the best fit model with normalisation  $\sigma_8 = 0.9$  shown in Fig. 7, the contribution of this data point to the chi-squared of the PS measurements ( $\chi^2 = 10.4$ ) is  $\Delta\chi^2 = 2.86$ , smaller than that of the data point at  $k = 0.00713 \text{ s km}^{-1}$ , for which  $\Delta\chi^2 = 4.45$ . We found indeed that the removal of this data point from the chi-squared does not affect the results noticeably.

Continuum fitting errors are likely to affect the flux probability distribution. The modelling of these errors is complicated by the fact that the scales of interest are of the order of the box size  $L$  of the simulations. However, M00 were able to demonstrate that, if the inclusion of continuum fitting errors can account for most of the discrepancy between the simulated and observed PDF in the range  $F \gtrsim 0.8$ , it should not affect much the PDF for  $F \lesssim 0.8$ . We thus believe that the PDF in the range  $F \lesssim 0.8$  is robust to these errors. Continuum fitting errors might also affect the inferred column densities  $N_{\text{HI}}$ . Notwithstanding, the deviation from a single power-law in the regime  $N_{\text{HI}} \lesssim 10^{14} \text{ cm}^{-2}$  is most probably caused by line blending, and by the non-linear evolution of the structures associated to the absorption

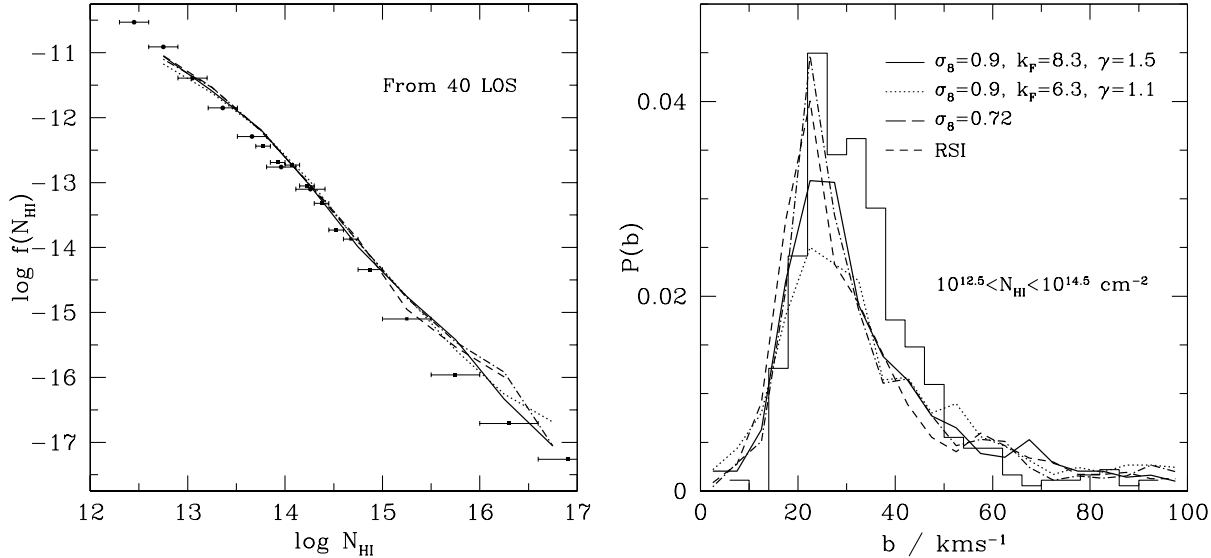


**Figure 11.** Left panel : The differential column density distribution  $f(N_{\text{HI}})$  of various models which fit the PS and PDF data best : two scale-invariant models of normalisation  $\sigma_8 = 0.9$  (solid and dotted-dashed curve), a scale-invariant model with  $\sigma_8 = 0.72$  (long-dashed curve), and a RSI model (short-dashed curve). The parameter values of these models are  $(k_F, \langle F \rangle, \gamma, \hat{T}_4) = (8.3, 0.69, 1.5, 1.5), (6.3, 0.69, 1.1, 1.5), (10.0, 0.7, 1.5, 1.5)$  and  $(12.5, 0.7, 1.1, 2)$  respectively. Note that the scale-invariant models have a temperature  $\hat{T}_4 = 1.5$ , while the RSI model has  $\hat{T}_4 = 2$ . The filled circles and squares are the data of Hu *et al.* (1995) and Petitjean *et al.* (1993) respectively. Right panel : the corresponding line-width distribution  $f(b)$ . Only the lines with column density  $N_{\text{HI}} = 10^{12.5} - 10^{14.5} \text{ cm}^{-2}$  were taken into account. The simulated distributions are compared to the data of Hu *et al.* (1995) shown as an histogram.

systems (e.g. Kim *et al.* 2002; see also Schaye 2001). Finally, continuum fitting errors should play a minor role in the flux power spectrum as the scales probed by our simulations are relatively small,  $k \gtrsim 0.003 \text{ s km}^{-1}$  (e.g. Kim *et al.* 2004).

Up to now we have adopted the prior  $\langle F \rangle = 0.684 \pm 0.023$  (M00). However, one should bear in mind that the presence of metal lines or strong absorption systems can substantially affect the determination of  $\langle F \rangle$  (e.g. Schaye *et al.* 2003; Viel *et al.* 2004b). In particular, Schaye *et al.* (2003) found that accounting for strong H $\alpha$  systems and metal lines yields a lower value of  $\langle F \rangle = 0.637$  at  $z = 3$ . Furthermore, as shown by Seljak, McDonald & Makarov (2003) and Viel, Haehnelt & Springel (2004), a wrong estimate of the mean flux level can severely bias the results. It is therefore prudent to examine to which extent the assumed mean flux level affects the results. For this purpose, we have repeated the analysis of Section §4.3.2 with a mean flux  $\langle F \rangle = 0.637$  (Schaye *et al.* 2003), and a standard deviation  $\sigma_F = 0.030$ . Only the diagonal elements of the PDF error matrix were considered in the chi-squared minimization. Furthermore,  $\Delta\chi^2$  was calculated from the PS data alone, and from the whole PS+PDF data set. We found that, in both cases, lowering the mean flux level amounts to a larger best fit value of  $\sigma_8$ , in agreement with previous studies (e.g. Viel, Haehnelt & Springel 2004). However, the effect is much weaker when  $\Delta\chi^2$  is computed from the whole PS+PDF data set ( $\lesssim 3\%$ ) than from the PS data alone ( $\lesssim 8\%$ ). Combining the flux PS measurements with other statistics of the Ly $\alpha$  forest can thus significantly reduce the sensitivity of the results to the mean transmitted flux.

Our semi-analytical model of the Ly $\alpha$  forest allows us to explore a much larger parameter space than full hydrody-

nodynamical simulations. However, the model has several shortcomings. It neglects any possible scatter in the temperature-density relation of the low density IGM as a result of shocks and patchy helium reionization (e.g. Gleser *et al.* 2005). It also assumes a filtering length that is independent of the local gas density and temperature. It also ignores any galactic feedback (e.g. Croft *et al.* 2002a; Kollmeier *et al.* 2003). Hydrodynamical simulations predict that shock heating should drive a significant fraction of the baryons into the warm-hot phase of the intergalactic medium (WHIM) at low redshift. At the present epoch, this fraction might be as large as 40% (e.g. Cen & Ostriker 1999; Davé *et al.* 2001; see also Nath & Silk 2001). At redshift  $z \sim 3$ , however, this fraction falls below 10%. Moreover, numerical simulations also show that most of the WHIM baryons at that redshift resides in overdensities  $\delta_g \gtrsim 10$  (Davé *et al.* 2001). Hence, shock heating should have a rather weak impact on the low density IGM at  $z \approx 3$ . Inhomogeneities in the UV background might also affect the flux power spectrum. Yet this effect should not be too important on the scales ( $k \gtrsim 0.05 \text{ s km}^{-1}$ ) and redshifts ( $z = 3$ ) of interest (e.g. Croft 2004; McDonald *et al.* 2004c). Recent measurements of the Ly $\alpha$  absorption near Lyman-break galaxies (Adelberger *et al.* 2003) are taken as evidence for the existence of dilute and highly ionized gas bubbles caused by supernovae-driven winds. Notwithstanding, simulations indicate that their small filling factor results in a moderate impact on statistics of the Ly $\alpha$  forest such as the power spectrum or the PDF (e.g. Croft *et al.* 2002a; Weinberg *et al.* 2003; Desjacques *et al.* 2004; McDonald *et al.* 2004c). Gleser *et al.* (2005) have demonstrated that patchy helium II reionization can cause significant scatter in the temperature density relation. A detailed account

**Table 3.** Parameter values of the models which best fit the flux PS and PDF, assuming a temperature-dependent smoothing  $k_F \hat{T}_g^{1/2} = \text{const}$ . The values listed in the upper half of the table were obtained using only the diagonal terms of the PDF error matrix whereas, in the lower half, they were obtained using the full covariance matrix of the flux PDF. The filtering scale  $k_F(1)$  is given in unit of  $h\text{Mpc}^{-1}$ . The adiabatic index has a fixed value  $\gamma = 1.3$ , while the mean IGM temperature is  $\hat{T}_4 = 1, 1.5$  and  $2$ . The last columns gives the best fit values of  $\langle F \rangle$ ,  $\sigma_8$  and the corresponding  $\chi^2$  (for 24 degrees of freedom).

filtering	$\gamma$	$\hat{T}_4$	$\langle F \rangle$	$\sigma_8$	$\chi^2$
$k_F(1) = 10$	1.3	1	0.68	0.67	24.9
		1.5	0.69	0.72	21.7
		2	0.69	0.76	25.3
$k_F(1) = 8$	1.3	1	0.68	0.84	22.4
		1.5	0.68	0.94	25.4
		2	0.68	0.93	38.7
$k_F(1) = 10$	1.3	1	0.70	0.70	26.9
		1.5	0.71	0.72	23.9
		2	0.71	0.72	27.7
$k_F(1) = 8$	1.3	1	0.71	0.83	23.8
		1.5	0.71	0.82	27.3
		2	0.71	0.88	38.1

of the effect of this scatter on the estimation of cosmological parameters has not yet been taking into account neither in semi-analytic modeling nor in hydrodynamical simulations. A constant filtering length also lead to systematic errors in the inferred values of  $\sigma_8$  (e.g. Viel, Haehnelt & Springel 2004). In any case all of these effects are not expected to amount to more than an error of 20% in the estimated best fit parameters.

## 5 DISCUSSION

We have used N-body simulations of variants of the  $\Lambda\text{CDM}$  models to generate synthetic spectra of the Ly $\alpha$  forest. We have simulated the standard  $\Lambda\text{CDM}$  cosmology with scale-invariant spectral index models, as well as a running spectral index model (Spergel *et al.* 2003). The one-dimensional flux power spectrum (PS) and flux probability distribution function (PDF) have been computed from mock catalogs, and compared to the observational data in order to constrain the cosmological models and the physical parameters that dictate the properties of the Ly $\alpha$  forest. In addition to the one- and two-point correlations, we have also computed the neutral hydrogen column density distribution and the line width distribution. These last two statistics have only been used as a consistency check for the models which give the best fit to the observed PS and PDF.

The RSI model matches the PS somewhat better than our scale-invariant model with rms fluctuation  $\sigma_8 = 0.9$ , but overestimates the PDF in the range  $F \gtrsim 0.6$  unless the temperature is very high,  $\hat{T}_4 \gtrsim 2$ . A scale-invariant model with  $\sigma_8 = 0.9$  matches better the flux PDF but tends to overestimate  $\Delta_F^2(k)$  on scale  $k \lesssim 0.01 \text{ s km}^{-1}$  when the temperature is large,  $\hat{T}_4 \gtrsim 1.5$ . However, the agreement with the observed flux power spectrum can be improved by lowering the value

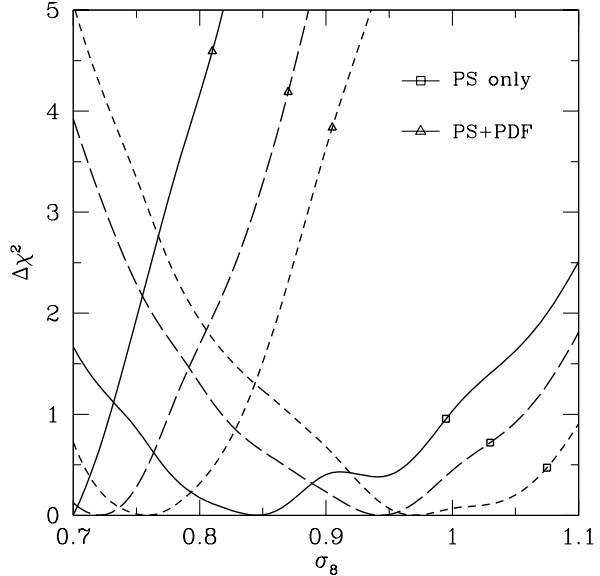


**Figure 12.** A comparison between the  $\Delta\chi^2$  versus  $\sigma_8$  computed from the PS alone (curves with squares), and from the PS+PDF data (curves with triangles).  $\Delta\chi^2$  was obtained after varying  $\sigma_8$  and  $\langle F \rangle$ , and marginalizing over the value of the mean flux. The mean IGM temperature is  $\hat{T}_4 = 1$  (solid curves),  $1.5$  (long-dashed) and  $2$  (short-dashed). The filtering is  $k_F = 10 h\text{Mpc}^{-1} \hat{T}_4^{-1/2}$  (cf. Section §4.3.2), and the adiabatic index has a fixed value  $\gamma = 1.3$ . The spline interpolation was performed using the diagonal elements of the PDF covariance matrix solely.

of the normalization amplitude,  $\sigma_8$ . Most importantly, models which match best the PS data alone usually do not yield a good fit to the PDF. The discrepancy worsens with decreasing temperature. In the case of the  $\sigma_8 = 0.9$ , scale-invariant cosmology, the disagreement with the observed PDF is particularly severe for  $\hat{T}_4 \gtrsim 2$ . We also computed the line statistics for some of our best fit models. We found that they all reproduce successfully the slope and normalisation of the column density distribution  $f(N_{\text{HI}})$ , as well as the overall line-width distribution  $f(b)$ . The simulated line-width distribution is probably affected by resolution effects. Yet the constraints on the primordial power spectrum are insensitive to the details of the line-width statistic. Degeneracies among the parameters diminish the ability of the data to constrain the shape and normalisation of the primordial power spectrum (e.g. Zaldarriaga, Hui & Tegmark 2001; Zaldarriaga, Scoccimarro & Hui 2003). In this respect, we have found that the pairs  $\gamma$  -  $k_F$  and  $\hat{T}_g$  -  $\sigma_8$  are degenerate when we marginalize over the mean transmitted flux. To proceed further, we have assumed that the filtering wavenumber  $k_F$  is related to the IGM temperature according to  $k_F \propto \hat{T}_4^{-1/2}$ . The reasons which motivate this choice are discussed in Appendix §A. Under that assumption, a chi-squared minimization indicates that the normalisation amplitude is likely to be  $0.7 \lesssim \sigma_8 \lesssim 0.9$  for a reasonable reionization scenario and temperatures  $1 \lesssim \hat{T}_4 \lesssim 2$ . For  $\hat{T}_4 \gtrsim 1.5$ , the data favour models with normalisation  $\sigma_8 \lesssim 0.8$  rather than models with  $\sigma_8 \gtrsim 0.8$ , the latter slightly overestimating  $\Delta_F^2(k)$  in the range  $k \lesssim 0.01 \text{ s km}^{-1}$ . It should also be noted that taking into ac-

count the full error matrix of the flux PDF systematically lowers the best fit values of  $\sigma_8$  by a few percents.

Our results suggest that the constraints inferred from measurements of the flux power spectrum alone might be biased. Most previous estimates of  $\sigma_8$  from Ly $\alpha$  absorption measurement relied on the flux PS alone (e.g. Croft *et al.* 1999, 2002; McDonald *et al.* 2000, 2004b; Viel, Haehnelt & Springel 2004; see also Viel, Weller & Haehnelt 2004; Seljak *et al.* 2004). In light of our results however, it is unclear whether their best fit models also match the PDF of the flux (and other statistics of the Ly $\alpha$  forest as well). To emphasize the importance of combining several statistics we compare in Fig. 12 the constraints on  $\sigma_8$  obtained from the PS data alone (curves with square) to those from the whole PS+PDF data set (curves with triangles). We assumed a filtering wavenumber of  $k_F = 10\hat{T}_4^{-1/2} h\text{Mpc}^{-1}$ . The curves  $\Delta\chi^2$  were calculated for a mean IGM temperature  $\hat{T}_4 = 1$  (solid curves), 1.5 (long-dashed) and 2 (short-dashed), but for a fixed adiabatic index  $\gamma = 1.3$ . Note that the best fit values of  $\sigma_8$  in the case of the PS data only are consistent with those inferred in previous works. Fig. 12 clearly demonstrates that the inclusion of the PDF in the minimization has a large impact on the normalisation amplitude, decreasing the best fit value of  $\sigma_8$  by about 20%. Consequently, the analysis of Viel, Haehnelt & Springel (2004) and McDonald *et al.* (2004b) may overestimate the normalisation amplitude. Furthermore, including the PDF significantly improves the confidence on  $\sigma_8$  as we can see from the shape of  $\Delta\chi^2$ . Finally, as we discussed in Section §4.5, it also noticeably reduces the sensitivity of the results to the mean flux level  $\langle F \rangle$ . A joint fit of the flux power spectrum and PDF can thus greatly improve over the standard analysis based on the flux power spectrum alone.

Although including the flux PDF tends to lower the best fit value of  $\sigma_8$ , overall our result of  $\sigma_8 = 0.85 - 0.95$  is consistent with the studies of Viel, Haehnelt & Springel (2004), and McDonald *et al.* (2004b). Both of these studies were based on flux measurements at several redshifts (McDonald *et al.* 2004b use eleven redshift bins spanning the range  $2.2 \leq z \leq 4.2$ ). They also relied on a more detailed treatment of the gas physics by means of hydrodynamical simulations. Our assumption of uniform smoothing does not account for the dependence of the smoothing on the local IGM density and temperature. Yet the exact relation between the gas and dark matter depends on the rather poorly constrained thermal and reionization history of the universe. Simulations incorporating a wider variety of reionization histories are needed for a better understanding of the systematics in inferring the cosmological parameters from the forest. It is also unclear whether the currently available hydrodynamical simulations give reasonable flux PDFs.

We have demonstrated that a joint analysis of the forest can potentially yield more robust estimates of the cosmological parameters than those inferred from the flux power spectrum alone. Here we have included mainly the PDF and the flux power spectrum. But other statistical measures can also be used. The flux bispectrum (e.g. Mandelbaum *et al.* 2003) offers a promising possibility as it should be less sensitive to systematics than the PDF.

## 6 ACKNOWLEDGEMENT

We thank Patrick McDonald and our referee, Joop Schaye, for many valuable comments on an earlier version of this manuscript. We acknowledge stimulating discussions with Martin Haehnelt, Michael Rauch, Ravi Sheth, David Tytler, and Matteo Viel. This Research was supported by the German Israeli Foundation for Scientific Research and Development, the EC RTN network “The Physics of the Intergalactic Medium”, and the United States-Israel Bi-national Science Foundation (grant # 2002352). VD would like to acknowledge the Institute of Astronomy (Cambridge) and The University of Pittsburgh where part of this work was accomplished.

## REFERENCES

Bahcall J.N., Salpeter E.E., 1965, ApJ, 142, 1677  
 Bennett C.L. *et al.* , 2003, ApJS, 148, 1  
 Bi H.G., 1993, ApJ, 405, 479  
 Bi H.G., Börner G., Chu Y., 1992, A&A, 266, 1  
 Bi H.G., Davidsen A.F., 1997, ApJ, 479, 523  
 Bryan G.L., Machacek M., Anninos P., Norman M.L., 1999, ApJ, 517, 13  
 Burles S., Tytler D., 1998, ApJ, 499, 699  
 Carswell R.F., Webb J.K., Cooke A.J., Irwin M.J., 2003, Voigt  
 Profile Fitting Program Version 5. Available on-line at  
<http://www.ast.cam.ac.uk/rfc/vpfit.html>  
 Cen R., Miralda-Escudé J., Ostriker J.P., Rauch M., 1994, ApJ, 437, L83  
 Cen R., Ostriker J.P., 1999, ApJ, 519, L109  
 Coles P., Jones B., 1991, MNRAS, 248, 1  
 Croft R.A.C., Weinberg D.H., Katz N., Hernquist L., 1998, ApJ, 495, 44  
 Croft R.A.C., Weinberg D.H., Pettini M., Hernquist L., 1999,  
 ApJ, 520, 1  
 Croft R.A.C., Hernquist L., Springel V., Westover M., White M.,  
 2002a, ApJ, 580, 634  
 Croft R.A.C., Weinberg D.H., Bolte M., Burles S., Hernquist L.,  
 Katz N., Kirkman D., Tytler D., 2002b, ApJ, 581, 20  
 Croft R.A.C., 2004, ApJ, 610, 642  
 Davé R. *et al.* , 2001, ApJ, 552, 473  
 Desjacques V., Nusser A., Haehnelt M.G., Stoehr F., 2004 MN-  
 RAS, 350, 879  
 Eisenstein D.V., Hu W., 1999, ApJ, 511, 5  
 Gleser L., Nusser A., Benson A.J., Ohno H., Sugiyama N., 2005,  
 ArXiv Astrophysics e-prints, astro-ph/0412113  
 Gnedin N.Y., Hui L., 1998, MNRAS, 296, 44  
 Gnedin N.Y., Hamilton A.J.S., 2002, MNRAS, 334, 107  
 Gnedin N.Y. *et al.* , 2003, ApJ, 583, 525  
 Gunn J.E., Peterson B.A., 1965, ApJ, 142, 1633  
 Hernquist L., Katz N., Weinberg D.H., Miralda-Escudé J., 1996,  
 ApJ, 457, L51  
 Hu E.M., Kim T.-S., Lennox L.C., Songaila A., Rauch M., 1995,  
 AJ, 110, 1526  
 Hui L., Gnedin N.Y., 1997, MNRAS, 292, 27  
 Hui L., Gnedin N.Y., Zhang Y., 1997, ApJ, 486, 599  
 Hui L., Burles S., Seljak U., Rutledge R.E., Magnier E., Tytler  
 D., 2001, ApJ, 552, 15  
 Katz N., Weinberg D.H., Hernquist L., 1996, ApJS, 105, 19  
 Kim T.-S., Hu E.M., Cowie L.L., Songaila A., 1997, AJ, 114, 1  
 Kim T.-S., Carswell R.F., Cristiani S., D’Odorico S., Giallongo  
 E., 2002, MNRAS, 335, 555  
 Kim T.-S., Viel M., Haehnelt M.G., Carswell R.F., Cristiani S.,  
 2004, MNRAS, 347, 335

Kollmeier J.A., Weinberg D.H., Davé R., Katz N., 2003a, ApJ, 594, 75  
 Mandelbaum R., McDonald P., Seljak U., Cen R., 2003, MNRAS, 344, 776  
 Matarrese S., Mohayaee R., 2002, MNRAS, 329, 37  
 McDonald P., Miralda-Escudé J., Rauch M., Sargent W.L.W., Barlow T.A., Cen R., Ostriker J.P., 2000, ApJ, 543, 1  
 McDonald P., Miralda-Escudé J., Rauch M., Sargent W.L.W., Barlow T.A., Cen R., 2001, ApJ, 562, 52  
 McDonald P., Miralda-Escudé J., 2001, ApJ, 549, L11  
 McDonald P., 2003, ApJ, 585, 34  
 McDonald P. et al. , 2004a, ArXiv Astrophysics e-prints, astro-ph/0405013  
 McDonald P. et al. , 2004b, ArXiv Astrophysics e-prints, astro-ph/0407377  
 McDonald P., Seljak U., Cen R., Bode P., Ostriker J.P., 2004c, ArXiv Astrophysics e-prints, astro-ph/0407378  
 McGill C., 1990, MNRAS, 242, 544  
 Miralda-Escudé J., Cen R., Ostriker J.P., Rauch M., 1996, ApJ, 471, 582  
 Nath B.B., Silk J., 2001, MNRAS, 327, 5  
 Nusser A., Haehnelt M.G., 2000, MNRAS, 313, 364  
 Nusser A., 2000, MNRAS, 317, 902  
 Peebles P.J.E., 1984, ApJ, 277, 470  
 Petitjean P., Webb J.K., Rauch M., Carswell R.F., Lanzetta K., 1993, MNRAS, 262, 499  
 Petitjean P., Mücket J.P., Kates R.E., 1995, A&A, 295, L9  
 Press W.H., Rybicki G.B., Schneider D.P., 1993, ApJ, 414, 64  
 Rauch M. et al. , 1997, ApJ, 489, 7  
 Rauch M., 1998, ARA&A, 36, 267  
 Reisenegger A., Miralda-Escudé J., 1995, ApJ, 449, 476  
 Ricotti M., Gnedin N.Y., Shull J.M., 2000, ApJ, 534, 41  
 Schaye J., Theuns T., Rauch M., Efstathiou G., Sargent W.L.W., 2000, MNRAS, 318, 817  
 Schaye J., 2001, ApJ, 559, 507  
 Schaye J., Aguirre A., Kim T.-S., Theuns T., Rauch M., Sargent W.L.W., 2003, ApJ, 596, 768  
 Seljak U., McDonald P., Makarov A., 2003, MNRAS, 342, L79  
 Seljak U. et al. , 2004, ArXiv Astrophysics e-prints, astro-ph/0407372  
 Spergel D.N. et al. , 2003, ApJS, 148, 175  
 Springel V., Yoshida N., White S.D.M., 2001, New Astronomy, 6, 79  
 Tegmark M., Zaldarriaga M., 2000, ApJ, 544, 30  
 Theuns T., Leonard A., Efstathiou G., Pearce F.R., Thomas P.A., 1998, MNRAS, 301, 478  
 Tytler D., 1987, ApJ, 321, 49  
 Viel M., Matarrese S., Heavens A., Haehnelt M.G., Kim T.-S., Springel V., Hernquist L., 2004a, MNRAS, 347, L26  
 Viel M., Haehnelt M.G., Carswell R.F., Kim T.-S., 2004b, MNRAS, 349, L33  
 Viel M., Haehnelt M.G., Springel V., 2004, MNRAS, 354, 684  
 Viel M., Weller J., Haehnelt M.G., 2004, MNRAS, 355, L23  
 Weinberg D.H., Romeel D., Katz N., Kollmeier J., 2003, AIP Conf. Proc., 666, 157  
 Zaldarriaga M., Hui L., Tegmark M., 2001, ApJ, 557, 519  
 Zaldarriaga M., Scoccimarro R., Hui L., 2003, ApJ, 590, 1  
 Zhang Y., Anninos P., Norman M.L., 1995, ApJ, 453, L57

## APPENDIX A: THE FILTERING LENGTH

Gas pressure smoothes the gas distribution relative to that of the dark matter. This effect becomes important below a (comoving) scale  $x_J = 1/k_J$ , the Jeans scale, which is defined as (e.g. Bi, Börner & Chu 1992)

$$x_J = \frac{1}{aH} \sqrt{\frac{2\gamma k_B \hat{T}_g}{3\mu m_p}} = 0.176 h^{-1} \text{Mpc} \left( \frac{\gamma \hat{T}_4}{1+z} \right)^{1/2}, \quad (\text{A1})$$

where  $a$  is the scale factor,  $H$  the Hubble constant,  $k_B$  the Boltzmann constant and  $\mu$  the mean molecular weight. Here,  $\gamma$  describes the temperature-density relation,  $T_g = \hat{T}_g(1 + \delta_g)^{\gamma-1}$ . The numerical estimate was obtained for a  $\Lambda$ CDM cosmology with matter content  $\Omega_m = 0.3$ , assuming  $\mu = 0.59$ , a value appropriate for a fully ionized plasma of primordial abundance. We should emphasize that eq. (A1), which defines the Jeans scale  $x_J(t)$  in term of physical quantities evaluated at mean density, merely defines a characteristic scale. The filtering scale  $x_F(\mathbf{x}, t)$  over which the IGM is smoothed will generally differ from the Jeans scale. For the moment, let us consider the filtering length at mean density,  $1/\hat{k}_F$ , which is also a function of time alone. The redshift evolution of  $\hat{k}_F$  is complex, and depends on the details of the reionization scenario, i.e. on the whole time evolution of  $k_J$ . However, for some particular choices of reionization history (e.g. sudden reionization), it is possible to work out analytic solutions to the linear equation governing the evolution of baryonic and dark matter in a EdS Universe (e.g. Peebles 1984; Bi, Börner & Chu 1992; Gnedin & Hui 1998; Nusser 2000; Matarrese & Mohayaee 2002). Under these assumptions, Gnedin & Hui (1998) pointed out that, at redshift  $z = 3$ , the filtering length (at mean density) is  $\hat{k}_F = \eta k_J$ , with  $\eta \sim 1.5 - 2.5$  for realistic reionization scenarios. These values should nonetheless not be taken too seriously given the uncertainties in the relation between baryons and dark matter. Taking  $\gamma = 1.3$  and  $\hat{T}_4 = 1$  yields  $\hat{k}_F \approx 7\eta h\text{Mpc}^{-1}$ . Note that we divided  $\hat{k}_F$  by  $\sqrt{2}$  to account for our definition of the filter,  $W = \exp(-k^2/2k_F^2)$ , which reduces to  $\approx 1 - k^2/2k_F^2$  in the limit of large wavenumber.

In our analysis, we smooth the Fourier modes of the dark matter density field with a uniform Gaussian filter to obtain the gas density and velocity fields. In reality, we expect the filtering length  $x_F(\mathbf{x}, t)$  to be a function of space and time through the local temperature and density. To get some idea of this dependence, let us consider a spherical perturbation of physical radius  $r = x_F/(1+z)$ . On the one hand, the excess pressure will try to smooth out the perturbation on a timescale  $r/c_s$ , where  $c_s$  is the local speed of sound. On the other hand, the enhanced density gives rise to an extra inward gravitational force (mainly due to dark matter) which tends to increase the matter content of the perturbation on a timescale  $1/\sqrt{G\rho_m^{\text{th}}}$ , where  $\rho_m^{\text{th}}$  is the dark matter density smoothed with a top-hat window of comoving width  $x_F$ . Equating these two timescales allows us to express  $x_F$  as

$$x_F = \frac{c_s}{\sqrt{G\rho_m^{\text{th}}}} (1+z). \quad (\text{A2})$$

The density  $\rho_m^{\text{th}}$  is not equal to the gas density. However, both are tightly related and have similar dependence on  $x_F$ . Hence, if we assume that  $\rho_m^{\text{th}} \propto \rho_g$ , and that the gas temperature and density follow the power-law relation discussed above, we have

$$x_F(z, \delta_g) = \hat{x}_F(z) (1 + \delta_g)^{\gamma/2-1}, \quad (\text{A3})$$

where  $\hat{x}_F(z)$  is the filtering length at mean density. For an adiabatic index  $1 \lesssim \gamma \lesssim 1.6$ , eq. (A3) implies that  $x_F$  depends weakly on the gas density contrast  $\delta_g$ . Notwithstanding, a

uniform smoothing will lead to an overestimation (underestimation) of the gas density in the low (high) density regions of the simulation. We can however adjust the strength of the  $k$ -space smoothing  $W$ , i.e. the value of  $k_F$ , such that the smoothed dark matter power spectrum is as close as possible to the true gas power spectrum. This is indeed the best we can do since it is practically impossible to mimic a non-uniform smoothing in real space with a  $k$ -space kernel.

To determine the optimal  $k_F$ , we assume that the gas density can be obtained locally from the dark matter density as follows :

$$1 + \delta_g(\mathbf{x}) = \int \frac{d^3y}{(2\pi)^{3/2}x_F^3} [1 + \delta_m(\mathbf{y})] e^{-\frac{(\mathbf{x}-\mathbf{y})^2}{2x_F^2}}. \quad (A4)$$

In principle, the filtering length  $x_F = x_F(\delta_g)$  should depend on the local gas density, and eq. (A4) would implicitly define  $\delta_g$ . For simplification however, we will assume that  $x_F = x_F(\delta_m) = \hat{x}_F(1 + \delta_m)^{\gamma/2-1}$  (equation A3). The Fourier transform of the gas density field is simply given by

$$\delta_g(\mathbf{k}) + \delta_D(\mathbf{k}) = \int \frac{d^3x}{(2\pi)^3} [1 + \delta_m(\mathbf{x})] e^{-\frac{1}{2}k^2x_F^2} e^{-i\mathbf{k}\cdot\mathbf{x}}, \quad (A5)$$

where  $\delta_D(\mathbf{k})$  is the Dirac delta function. The gas power spectrum is then (ignoring the term at  $\mathbf{k} = 0$ )

$$P_g(\mathbf{k}) = \int \frac{d^3r}{(2\pi)^3} \langle (1 + \delta_m) (1 + \delta'_m) e^{-\frac{1}{2}k^2(x_F^2 + x'_F^2)} \rangle e^{-i\mathbf{k}\cdot\mathbf{r}}, \quad (A6)$$

where the fields  $\delta_m$ ,  $x_F$  and  $\delta'_m$ ,  $x'_F$  are evaluated at position  $\mathbf{x}$  and  $\mathbf{x} + \mathbf{r}$  respectively.  $P_g(\mathbf{k})$  is thus the Fourier transform of a mass-weighted filter,

$$\mathcal{Z}_g[k, \mathbf{r}] = \langle (1 + \delta_m) (1 + \delta'_m) e^{-\frac{1}{2}k^2(x_F^2 + x'_F^2)} \rangle. \quad (A7)$$

To estimate  $k_F$ , we consider the limit of small wavenumbers  $k \rightarrow 0$ . Since the integrand is weighted by  $r^2$ , we expect the main contribution to the integral to arise in the limit  $|\mathbf{r}| \rightarrow \infty$ . Expanding the previous equation to first order in  $k$  and taking the limit  $|\mathbf{r}| \rightarrow \infty$ , we have

$$\begin{aligned} \mathcal{Z}_g[k, \mathbf{r}] &\approx (1 + \xi_m(r)) - \frac{k^2}{2} \langle (1 + \delta_m) (1 + \delta'_m) (x_F^2 + x'_F^2) \rangle \\ &= (1 + \xi_m(r)) \left[ 1 - k^2 \frac{\langle (1 + \delta_m) (1 + \delta'_m) x_F^2 \rangle}{1 + \xi_m(r)} \right] \\ &\approx (1 + \xi_m(r)) \left[ 1 - k^2 \langle (1 + \delta_m) x_F^2 \rangle \right], \end{aligned} \quad (A8)$$

since the cross-terms  $\langle \delta'_m x_F^2 \rangle$  and  $\langle \delta_m x_F^2 \delta'_m \rangle$ , and the two-point correlation  $\xi_m$  tend to zero for large separation. Hence, in the limit  $k \rightarrow 0$ , the gas power spectrum can be expressed as

$$P_g(\mathbf{k}) \simeq \left( 1 - \frac{k^2}{k_F^2} \right) P_m(\mathbf{k}), \quad (A9)$$

where  $k_F$  is an effective filtering length which differs from the filtering length  $\hat{k}_F = 1/\hat{x}_F$  at mean density,

$$\frac{1}{k_F^2} = \langle (1 + \delta_m) x_F^2 \rangle = \frac{1}{\hat{k}_F^2} \int d\delta_m \mathcal{P}(\delta_m) (1 + \delta_m)^{\gamma-2}. \quad (A10)$$

Here,  $\mathcal{P}(\delta_m)$  is the one-point probability distribution of the dark matter density field. Eq. (A10) shows that, in the linear regime,  $k_F$  is obtained from a mass-weighted average of the local filtering length  $x_F$ . To evaluate  $k_F$ , we will assume that the dark matter PDF is well approximated by a lognormal distribution,

$$\mathcal{P}(\delta_m) d\delta_m = \frac{1}{\sqrt{2\pi}\sigma_L} e^{-\nu^2/2\sigma_L^2} d\nu. \quad (A11)$$

with  $\nu = \ln(1 + \delta_m) + \sigma_L^2/2$ , and where  $\sigma_L$  is the linear rms of dark matter fluctuations (Coles & Jones 1991). Although this approximation is inaccurate when  $\sigma_L \gtrsim 1$ , it should be adequate enough to assess whether  $k_F$  is larger or smaller than  $\hat{k}_F$ . The calculation yields

$$k_F^2 = \hat{k}_F^2 (1 + \sigma_{NL}^2)^{(\gamma-2)(3-\gamma)/2}, \quad (A12)$$

where we have used  $1 + \sigma_{NL}^2 = \exp(\sigma_L^2)$ . Note that, since  $x_F$  depends on the local gas density through relation (A3), we should expect  $\sigma_{NL}$  to be a smoothed version of the dark matter rms fluctuation amplitude, i.e. a function of  $k_F$ . Nonetheless, equation (A12) clearly shows that, for an adiabatic index  $1 \lesssim \gamma \lesssim 1.6$ , the mass-weighted filtering wavenumber  $k_F$  is smaller than that at mean density. This follows from the fact that most of the mass resides in moderately high-density regions where the temperature  $T_g$  is significantly larger than  $\hat{T}_g$  (e.g. Bi & Davidsen 1997). Consequently, given that i)  $\hat{k}_F \propto k_F$  and ii)  $k_F \leq \hat{k}_F$ , we can place an upper limit on the filtering  $k_F$ . For the particular choice  $\gamma = 1.3$ , one has  $k_F \lesssim 7\eta\hat{T}_4^{-1/2} h\text{Mpc}^{-1}$ . Bearing in mind that the IGM temperature is most probably larger than  $10^4$  K at  $z = 3$  (e.g. Schaye *et al.* 2000), we believe that  $k_F \lesssim 14 h\text{Mpc}^{-1}$  should be a reliable lower limit on the amount of filtering at  $z = 3$  for a reasonable history of the Universe.